Université Mohamed Khider – Biskra		**جامعة محمد خيضر بسكرة**
Faculté des Sciences et de la technologie		**كلية العلوم والتكنولوجيا**
Département: Chimie Industrielle		**قسم الكيمياء الصناعية**

جامعة محمد خيضر بسكرة

Thèse présentée en vue de

l'obtention du diplôme de : Doctorat LMD

Option : Génie chimique

Etude de l'influence de la vitesse de soudage par SMAW sur l'acier X42

Présentée par :

ABDERRAHMANI Safa

Soutenue publiquement le : **26/02/2025**

Devant le jury composé de :

MERZOUGUI Abdelkrim	**Professeur**	**U. de Biskra**	**Président**
CHÉRIFI Nedjema	**MCA**	**U. de Biskra**	**Rapporteur**
HAMDI Ines	**MCA**	**U. de Biskra**	**Examinateur**
ACHOURI Abderrahim	**Professeur**	**U. de Ouargla**	**Examinateur**

Mohamed Khider University – Biskra

Faculty of Sciences and Technology

Department: Industrial Chemistry

جامعة محمد خيضر بسكرة

كلية العلوم والتكنولوجيا

قسم الكيمياء الصناعية

جامعة محمد خيضر بسكرة

Thesis presented with a view to

obtaining the Diploma of

Doctorat LMD

Option: chemical engineering

Study of the Influence of SMAW Welding Speed on X42 Steel

Presented by :

ABDERRAHMANI Safa

Publicly supported on: **26/02/2025**

Before the jury composed of:

MERZOUGUI Abdelkrim	**Professor**	**U. of Biskra**	**President**
CHÉRIFI Nedjema	**Lecturer**	**U. of Biskra**	**Rapporteur**
HAMDI Ines	**Lecturer**	**U. of Biskra**	**Examiner**
ACHOURI Abderrahim	**Professor**	**U. of Ouargla**	**Examiner**

بِسْــــمِ

﴿يَرْفَعِ اللَّهُ الَّذِينَ آمَنُوا مِنكُمْ وَالَّذِينَ أُوتُوا الْعِلْمَ دَرَجَاتٍ ۚ وَاللَّهُ بِمَا تَعْمَلُونَ خَبِيرٌ﴾

الإهداء

الحمد لله وكفى، والصلاة والسلام على الحبيب المصطفى وآلة وصحبه ومن تبعه، أما بعد:

﴿ وَآخِرُ دَعْوَاهُمْ أَنِ الْحَمْدُ لِلَّهِ رَبِّ الْعَالَمِينَ ﴾

ما بدأنا المسيرة إلا بتوفيق الله، وما وصلنا إلى النهايات إلا بفضله، فالشكر لله حبًا وامتنانًا على البداية والنهاية ، فاللهم لك الحمد حتى ترضى، ولك الحمد إذا رضيت، ولك الحمد بعد الرضى.

بكل حب أهدي ثمرة نجاحي وتخرجي إلى:

الأيادي النقية التي أزالت من طريقي أشواك الفشل، إلى من غرسوا في الثقة والأمان، إلى أسرتي، الأرض الصلبة والدعم المستمر.

إلى من علموني أن الحياة رحلة كفاح وسلاحها العلم والمعرفة، إلى والدي العزيز الذي كان داعمي بلا حدود، وإلى والدتي الحبيبة التي تمثل لي مصدر القوة والدعم الدائم. إلى جميع أفراد عائلتي، جدتي وأخواتي وعمي وعماتي، الذين كانوا دائماً مصدر إلهام لي. حفظهم الله و رعاهم.

إلى صديقات العمر، إلى رفيقات الكفاح، من كنَّ في السنوات العجاف غيمةً ممطرةً، **الدكتورة نعيمة عزري وهاجر بركات.**

اعترافًا وتقديرًا مني بالجميل، أتقدم بجزيل الشكر **للدكتورة شريفي نجمة** التي لم تألُ جهدًا في تشجيعي على إتمام هذا البحث العلمي.

إلى من كان له الفضل في تعليمي منذ بداية مسيرتي التعليمية إلى نهايتها.

إلى كل شخص قريب كان أو بعيد شجعني وطمأنني وحول خوفي إلى أمان.

إليكم أهدي شكري وثمرة جهدي.

Thanks

Summary

Summary

Experimental part

Chapter III: materials and methods

Experimental part

Chapter IV: Discussion of results

Symbols List

Symbols	Meaning	unit
X70	the grade of the steel	
70	70 means: 70000 psi, this is the elastic limit of steel in psi"pound per square inch"	
HV	hardness vickers	
CFC	cubic face centered	
CC	centered cubic	
NF A 35-602	A component of the French National Standards, this standard delineates the criteria for categorizing and naming steel grades.	
Re	the yield strength	MPa
Rm	the tensile strength	MPa
A	the percentage of elongation after rupture	%
WZ	The weld zone	
HAZ	The heat affected zone	
MB	the base metal	
Ø	The diameter of the coated electrode	mm
E6010	The "E" denotes its classification as an electrode. The "60" designates a minimum tensile strength of 60,000 pounds per square inch. The designation indicates its suitability for all welding positions.	
E8010-P1	The "E" denotes its classification as an electrode. The "60" designates a minimum tensile strength of 60,000 pounds per square inch. The designation indicates its suitability for all welding positions, P1: Specially designated piping electrode	
JCPDS	Joint Committee on Powder Diffraction Standards	
HNO_3	nitric acid	
C_2H_5OH	ethanol	
hkl	are numbers that represent where the three axes of the crystallographic coordinate system intersect the crystal plane.	
K	Debye – Scherer's constant (0.94)	
λ	the wavelength of the CuKα radiation (0.154 nm)	

B	Full width half maximum (FWHM) of the peak	°2Th
θ	Bragg's angle samples	Degree°
δ	Dislocation density	nm^-2
TC(hkl)	Texture coefficient	
I(hkl)	Measured intensity of a specific crystallographic plane (hkl) in the sample	
I0(hkl)	Intensity of the same plane in a reference sample with random orientation.	
N	Number of reflections (planes) considered in the analysis.	
HB	Brinell hardness	HB
σut	Ultimate strength	MPa
σy	yield strength	MPa
D	Crystal siz	nm
S_1	First welding speed	m/s
S_2	Second welding speed	m/s
U	Tension electrique	V
I	welding currents	A
D	Crystal siz	nm

Figures list

Table List

Mathematical equations list

Abstract

Résumé

الملخص

Abstract

This study examines the impact of multi-pass hand welding speed on X42 steel joints using the Shielded Metal Arc Welding (SMAW) method. The focus is on how this speed affects the mechanical, metallurgical, and chemical properties of the steel. Two samples of X42 steel were welded at different speeds for comparison. The analyses included observations using a Scanning Electron Microscope (SEM), X-ray Diffraction (XRD) tests, and Vickers Hardness (Hv) tests. The results indicate that lower welding speeds, such as 20 mm/min, enhance crystalline stability, weld quality, and defect resistance. In contrast, higher speeds, such as 35 mm/min, lead to faster cooling, which may adversely affect the crystalline structure and increase dislocation density, potentially resulting in defects. Moreover, slower welding speeds allow for better grain development and optimized texture orientation, ensuring better control over the process. However, while higher speeds may increase productivity, they complicate the maintenance of welding consistency.

Keywords: Welding speed, X42 steel, SMAW, mechanical properties, SEM, XRD, Vickers hardness.

RÉSUMÉ

Cette étude analyse l'impact de la vitesse de soudage multi-passes à main libre sur les joints en acier X42 utilisant la méthode de soudage à l'arc sous protection (SMAW). L'accent est mis sur l'influence de cette vitesse sur les propriétés mécaniques, métallurgiques et chimiques de l'acier. Deux échantillons d'acier X42 ont été soudés à différentes vitesses pour effectuer une comparaison. Les analyses comprennent des observations au microscope électronique à balayage (MEB), des tests de diffraction des rayons X (DRX), et des essais de dureté Vickers (Hv). Les résultats montrent que des vitesses de soudage inférieures, comme 20 mm/min, favorisent une structure cristalline stable, une qualité de soudage améliorée et une meilleure résistance aux défauts. En revanche, des vitesses plus élevées, telles que 35 mm/min, entraînent un refroidissement rapide, perturbant ainsi la structure cristalline et augmentant la densité des dislocations, ce qui peut provoquer des défauts. De plus, des vitesses de soudage plus lentes permettent un meilleur développement des grains et une orientation optimisée de la texture, garantissant ainsi un meilleur contrôle du processus. Toutefois, bien que des vitesses plus rapides puissent accroître la productivité, elles compliquent le maintien de la cohérence du soudage.

Mots-clés : Vitesse de soudage, acier X42, SMAW, propriétés mécaniques, MEB, DRX, dureté Vickers.

الملخص

تتناول هذه الدراسة تأثير سرعة اللحام على الوصلات من الفولاذ X42 باستخدام طريقة لحام القوس الكهربائي تحت الحماية (SMAW). يتم التركيز على تأثير هذه السرعة على الخصائص الميكانيكية والمعدنية والكيميائية للفولاذ. تم لحام عينتين من الفولاذ X42 بسرعات مختلفة لإجراء مقارنة. شملت التحليلات ملاحظات باستخدام مجهر إلكتروني مسح (MEB)، واختبارات حيود الأشعة السينية (DRX)، واختبارات صلابة فيكرز (Hv). تشير النتائج إلى أن سرعات اللحام المنخفضة، مثل 20 مم/دقيقة، تعزز من استقرار البنية البلورية، وجودة اللحام، ومقاومة أفضل للعيوب. في المقابل، تؤدي السرعات العالية، مثل 35 مم/دقيقة، إلى تبريد أسرع، مما قد يؤثر سلبًا على البنية البلورية ويزيد من كثافة التشوهات، مما قد يؤدي إلى ظهور عيوب. علاوة على ذلك، تسمح سرعات اللحام الأبطأ بتطوير أفضل للحبيبات وتوجيه محسن للنسيج، مما يضمن تحكمًا أفضل في العملية. ومع ذلك، على الرغم من أن السرعات الأعلى قد تزيد من الإنتاجية، إلا أنها تعقد الحفاظ على اتساق اللحام.

الكلمات المفتاحية: سرعة اللحام، فولاذ X42، SMAW، الخصائص الميكانيكية، MEB، DRX، صلابة فيكرز

General
Introduction

General Introduction

The rapid population growth and continuous industrial expansion have led to a significant increase in the demand for petroleum products, often exceeding the available supply. This imbalance necessitates either the discovery of new resources or importing them from other regions. As a result, the transportation of crude oil and natural gas has become a major concern for the industrial sector, especially with the discovery of new resource sites. Pipelines are the preferred means for long-distance transport, and steel pipes are particularly valued for their strength, durability, and flexibility under low-temperature conditions. X42 steel is commonly used in oil and gas transmission systems due to its good mechanical properties and corrosion resistance, making it suitable for low to medium-pressure applications **(SH.Satish et al., 2017) (Özarpa et al., 2023).**

Failures in oil and gas pipelines can result in significant economic, environmental, human, and material losses. Algeria has witnessed several serious incidents, including the explosion in Boumerdès in 2004, which caused human casualties and extensive material damage. In 2018, Oran experienced a gas leak due to a failure in a transmission pipeline, leading to environmental hazards and cases of suffocation among nearby residents. In 2020, an explosion in a gas pipeline in Sidi Okba, Biskra, resulted in considerable material losses and a disruption of gas supplies to the region, in addition to environmental damage caused by the leak. Furthermore, several pipelines in southern Algeria have suffered from corrosion and leakage, affecting oil and gas transportation. These incidents highlight the critical importance of ensuring the safety and integrity of pipelines in Algeria**.**

Pipeline incidents arise from multiple factors, including corrosion, mechanical damage, natural events, human error, and the quality of welding. Welding is essential in the installation, upkeep, and repair of oil and gas pipelines. However, improper welding methods or flaws in welded connections can compromise pipeline integrity, creating vulnerabilities that may result in accidents. Key issues, such as substandard welding quality, incomplete fusion, inadequate penetration, and inappropriate material choices, are primary causes of welding-related failures **(M.Biezma et al., 2020)(K. Bijaya et al., 2020).**

This study investigates the influence of welding speed on the weld quality of X42 steel using the Shielded Metal Arc Welding (SMAW) process, a preferred method for its cost-effectiveness, ease of use, and low maintenance requirements compared to other methods. Weld quality is affected by several parameters, including current, voltage, and speed. This research focuses on how variations in welding speed the rate at which the electrode travels along the

joint impact weld outcomes. By examining the effect of welding speed on bead width and penetration, the study aims to identify optimal parameters that enhance the safety and reliability of welded joints in oil and gas pipelines **(Özarpa et al., 2023) (S. Farrukh et al., 2019) (P. Tewari et al., 2010).**

Samples of gas and oil transmission lines from Cosider's workshop in Biskra, welded using SMAW technique, were collected for analysis. Cosider, an Algerian company specializing in oil construction, large-scale infrastructure, and transportation projects. Prepared these samples through cutting and polishing. Mechanical testing was then conducted to measure Vickers hardness (HV), followed by microscopic analysis using X-ray diffraction (XRD) and scanning electron microscopy (SEM). The findings provide essential insights into the effects of welding speed on the steel's microscopic, mechanical, and chemical properties.

This thesis is divided into two parts, each consisting of two chapters, as follows:

Bibliographic part

Chapter I

The literature review offers essential background information on steel and its various classifications, with a specific emphasis on X42 steel.

Chapter II

This section provides an overview of the fundamentals, types, and applications of welding, with a focus on shielded metal arc welding (SMAW).

Experimental part

Chapter III

This chapter outlines the experimental procedures, including sample preparation steps like cutting, polishing, and chemical etching, along with the materials and methods used for chemical and mechanical characterization. These activities were conducted across three laboratories: the educational laboratory of metallurgy at the Faculty of Science and Technology at Mohamed Khider University of Biskra, the research and development laboratories, DCRD, Sonatrach, Boumerdes, and the Center for Scientific and Technical Research in Physical and Chemical Analysis, CRAPC, Biskra.

Chapter IV

This section presents the results and discusses the various methods used for characterization, including X-ray diffraction (XRD), Vickers hardness testing (HV), and scanning electron microscopy (SEM).

Data analysis was carried out using specialized software tools, such as Xpert HighScore Plus

for X-ray diffraction analysis and Mountains Software for surface data analysis.

This part includes the results of a study on the effect of shielded metal arc welding (SMAW) speed on X42 steel. Additionally, the same study was applied under identical conditions and variables to X70 steel for comparison purposes, without any changes in methodology or parameters.

The discussion concludes with a summary of the key findings derived from these analyses.

.

Bibliographic
Part

Chapter I
Basic information about steel

I Basic information about steel

I.1 Introduction

Steel is known for its exceptional hardness and resistance to various conditions, making it the material of choice for transporting hydrocarbons. Using steel pipes minimizes costs, reduces the risk of theft, and lessens the environmental impact associated with transporting hydrocarbons through pipelines.

In this chapter, we have discussed key concepts related to steel and its properties.

I.2 History of pipelines

The oil industry employs **X42 API 5L** pipelines for transporting oil and natural gas. Made from seamless hot-rolled tubing, these pipelines benefit from advancements in production techniques that have significantly enhanced their mechanical and structural properties, thus creating new opportunities for oil transport **(A. Mebrek et al., 2013).**

The use of pipes for transporting production from deposits dates back to 1865 in the United States. Since then, this method for moving liquid or gaseous hydrocarbons has gained global adoption, starting in the U.S. Regular transportation of liquefied natural gas began in 1964-1965, with shipments made between the Arzew liquefaction plant in Algeria and the LNG terminals in Canvey Island, UK, and Le Havre, France **(H.Féthi, 2013).**

Figure I.1: Gas and petroleum pipelines **(H.Féthi, 2013).**

I.3 Definition of steel

Steel is an alloy primarily composed of iron, with carbon content ranging from 0.02% to 2% by weight, which imparts its key properties. Other iron-based materials, such as cast iron and ferroalloys, differ in composition and characteristics, setting them apart from steel **(G. Tong et al., 2016).**

I.4 The different types of steels

Steel grades encompass various types primarily composed of iron and are categorized based on chemical composition or intended application. Application-based classification divides steel into four main groups: general-purpose carbon steels, heat-treated steels (with or without special treatments), tool steels, and stainless steels **(M.Hayat, 2017).**

I.5 Carbon steels: structures, properties

Non-alloy steels are represented in the Iron-Carbon diagrams (Figure I.2) based on their equilibrium structures **(Y.Houda, 2013).**
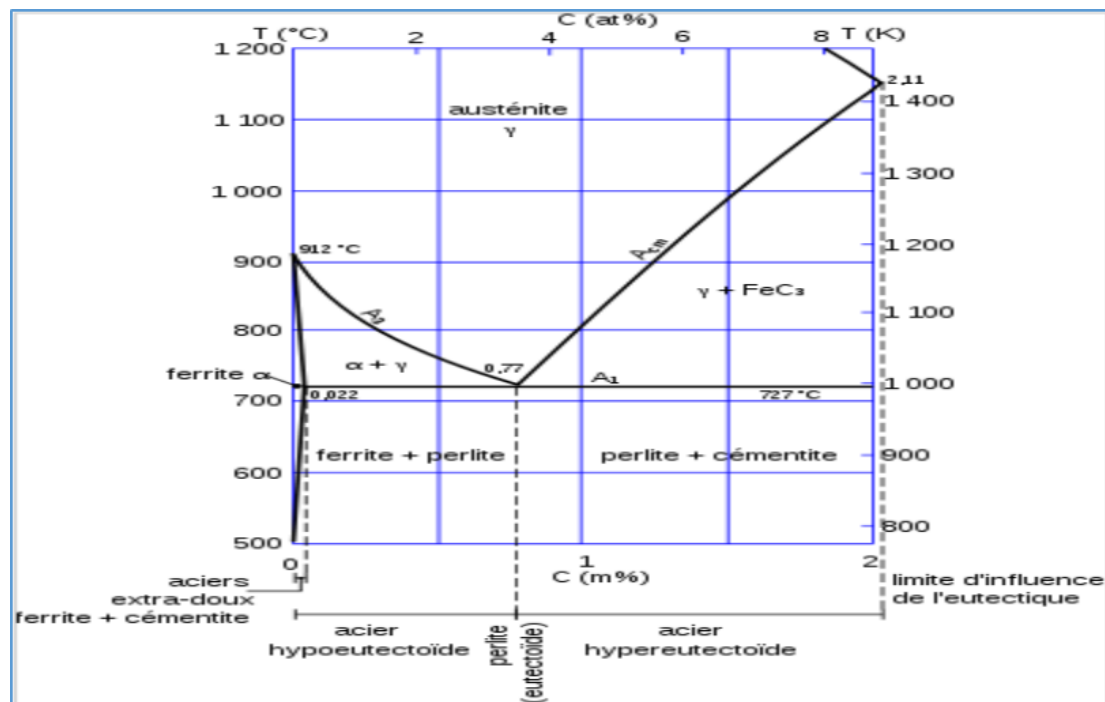
Figure I.2 : Iron-carbon equilibrium diagram **(Y.Houda, 2013).**
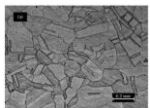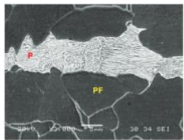
- Eutectoid steels, which usually contain about 0.8% carbon, are characterized by a fully pearlitic structure.

- Hypoeutectoid steels, with carbon content between 0.02% and 0.8%, consist of a structure comprising both ferrite and pearlite.

- Hypereutectoid steels, containing carbon levels from 0.8% to 1.5%, exhibit a structure made up of pearlite and primary cementite.

I.6 Basic characteristics of steels

Iron exists in two crystalline forms:

- **Body-Centered Cubic Iron (α iron):** Stable below 910°C and above 1400°C, and

- **Face-Centered Cubic Iron (γ iron):** Stable between 910°C and 1400°C. Solid solutions of γ iron are known as austenite. The iron-carbon equilibrium diagrams help classify alloying elements into two categories:

- **Austenite Stabilizers (Type A):** Which facilitate the transformation between α and γ forms and raise the temperature at which γ transforms into δ.

- **Ferrite Stabilizers (Type B):** Which can shift the melting range and the domain of α + γ to lower temperatures, affecting the stability of ferrite and the γ + δ domain **(M.Hichem, 2017).**

Table I.1 : Metallographic equilibrium constituents **(R. Bodlos, 2018).**

A	**Austenite** The solid cubic close-packed (CFC) solution of carbon in γ-iron (austenite) is a ductile phase of iron that remains stable only above the A_1 temperature line in non-alloy steels.	
B	**Ferrite** Solid solution CC of carbon in slightly hard ductile α-iron (Re=300 MPa, HV=80, A=50%)	
C	**Perlite** Eutectoid mixture of about 88% Ferrite and 88% cementite In the form of alternating thin strips (Re = 800 MPa,HV=200, A=10%)	
	Cementite Compound defined Fe_3C.Iron carbide has orthorhompic crystalline structure. Very hard and fragile (HV=700, A-0%)	
D	**Ferrite+ Perlite** Hypoeutectic steels exhibit a characteristic mixture whose proportions vary with carbon content. During cooling, ferrite grains develop along the boundaries from austenite, particularly within the α + γ domain.	
E	**Perlite+ Cementite** Hypoeutectic steels have a characteristic microstructure with proportions that vary according to carbon content, yet the cementite content remains below 20% of the total steel composition. As cooling occurs, a cementite network develops along the austenite grain boundaries as it passes through the α + Fe_3C phase region.	
	Globular perlite (coalesced) The eutectic mixture formed at 727 °C undergoes globularization annealing at 700 °C, where cementite lamellae merge into a spheroidal shape, becoming slightly softer and more ductile than lamellar pearlite.	

I.7 The classes of stainless steel

According to the two standards NF A 35-602, stainless steels are classified as follows

```
                    The classes of stainless steel
```

Martensitic steels	Austenitic steels	Ferritic steels
These steels, with a cubic structure, contain 13% chromium and are produced by reheating stainless steel to a high temperature followed by rapid cooling, known as "quenching.	These steels typically contain 0.02% to 0.1% carbon, 17% to 20% chromium, 7% to 25% nickel, and 2% to 5% molybdenum. Nickel contributes to the austenitic structure and improves corrosion resistance.	They contain 11-29% chromium without nickel, cannot be soaked, and have a crystal structure similar to iron with a central cubic arrangement.

Figure I.3 : The classes of stainless steel **(G.Olfa, 2015).**

I.8 The various kinds of steels

- Steel grades are categorized according to their chemical composition or intended applications, leading to the identification of four main steel families: carbon steels for general purposes,
- All alloyed and heat-treated steels.
- All tool steels.
- Stainless steels **(M.Hayat, 2017).**

I.9 API 5L X42 Steel

API 5L X70 steel is a microalloyed steel widely utilized in building hydrocarbon pipelines, such as those for gas and oil. Its microstructure primarily consists of ferrite and pearlite. **(D.Boualem et al., 2020).**

I.9.1 API 5L X42 Steel properties

I.9.1.1 Mechanical properties

Table. I.2: Mechanical properties of API 5L X42 steel **(Karuhanga, 2010).**

Features API5L	Re (MPa)	Rm (MPa)	A(%)
X70	290-440	> 415	21

With:

- Re: Yield strength.
- Rm: Tensile strength.
- A%: Elongation percentage after fracture **(Karuhanga, 2010).**

I.9.1.2 Chemical composition

- ❖ Spectrometric Analysis: This involves measuring elemental wave emissions.
- ❖ X42 Steel: Low carbon (~0.24%), good strength-weldability balance, suitable for pipelines.

Chemical Composition: See detailed information in Table I **(Özarpa et al., 2023).**

Table. I.3: Chemical composition of X42 steel **(Özarpa et al., 2023).**

Element	C	Fe	Si	Mn	S	P	Cr	Ni	Mo	V	cu	Al	Nb
%	0.115	95-99	0.27	0.80	0.004	0.008	0.024	0.048	-	-	0.28	0.043	-

I.10 Effect of chemical composition of steel

Steel is composed of various chemical elements, and any increase or decrease in these elements can significantly impact its properties, as illustrated in the table below (**M. Ali et al., 2020**).

TableI.4: Effect of chemical composition of steel (**M. Ali et al., 2020**).

Element	Influences
Carbon (C)	- The increase in carbon levels in the steel improves the mechanical strength (Rm). - Improved stress on the elastic limit (Re). - Improves the hardness of steel (Hv). - Low ductility (Z). And so steel formation
Manganese (Mn)	Manganese is an essential element of low-grade steel alloys in carbon - It increases the elastic strength of the steel by 30 MPa for 1% by weight of manganese. - Detection of the locations of sulfur-containing elements (S) in the steel by formation of compound (Min S).
Molybdenum (Mo)	It is (Mo) the second element after carbon in the strengthening of iron - Raise the microscopic hardness of the steel. - Height of hardening of the structure between two temperatures (400°C_ 625°C). - Anti-oxidant and chemical corrosion.
Silicon (Si)	- High hardness steel (1.5-2) Kg/mm2 for 0.1% by weight of silicon
Aluminium (Al)	- Increases the oxidation resistance of steel. - It can interfere with some curing processes

Vanadium (V)	- Vanadium: Enhances steel hardness while maintaining elongation and flexibility. - Oxidizer: Improves steel quality through its active oxidizing properties. - Optimal Content: A range of 0.5% to 0.7% vanadium effectively transforms steel properties. - Benefits: Increases tensile strength and fatigue resistance, and reduces the risk of heating issues. - Heat Resistance: Helps prevent the formation of soft bands after heat treatment.

I.11 Nomenclature of steel X42

The designation API 5L X42 is one of the classifications used to define the properties of pipe steel according to the API 5L standard issued by the American Petroleum Institute. The "X" indicates that the steel is specifically designed for pipeline applications, classifying it as a high-strength, low-alloy steel (HSLA). The number "42" refers to the steel's yield strength, which is 42,000 psi (approximately 290 mega pascals). These properties make X42 steel suitable for applications that require medium pressure resistance, such as oil and gas pipeline systems.

- API 5L stands for: pipeline.
- X : Indicates that the steel is intended for pipeline applications.
- 42: Refers to the yield strength of the steel, which is 42,000 psi, equivalent to approximately 290 megapascals (MPa) "pound per square inch" (pound per square inch**) (Karuhanga, 2010) .**

Chapter II

General information about welding

Shielded Metal Arc Welding

(SMAW)

II General information about welding Shielded Metal Arc Welding (SMAW)

II.1 Introduction

Welding is an assembly technique aimed at creating a seamless connection within the materials being joined. In metal welding, this atomic-level continuity ensures that the components are physically cohesive. Ideally, interatomic forces and gradual diffusion promote the bonding of fully contacted metal surfaces. However, to achieve the desired level of continuity, it often becomes necessary to apply activation energy to accelerate the process **(K.Adnen, 2013).**

II.2 Welding processes

Welding is a technique used to permanently join materials, ensuring their continuity at the atomic level. Ideally, welding creates a seamless bond through interatomic forces and slow diffusion, requiring well-aligned, contaminant-free surfaces. However, activation energy is often needed to establish this bond quickly. As a manufacturing process, welding fuses or diffuses materials, typically metals or thermoplastics, through heat input, sometimes with the addition of filler metal. Continuous advancements in welding methods enhance the quality and reliability of welded joints.

In the energy sector, various types of steel are welded using arc welding processes, including Shielded Metal Arc Welding (SMAW), Tungsten Inert Gas (TIG) welding, Metal Inert Gas/Metal Active Gas (MIG/MAG) welding, and Submerged Arc Welding (SAW). Additionally, other methods such as resistance welding, friction welding, plasma welding, laser welding, and ultrasonic welding are employed in advanced applications that require high precision and efficiency. The details of these processes and their parameters are illustrated in Figure II.1**(L.Shibo, 2017).**
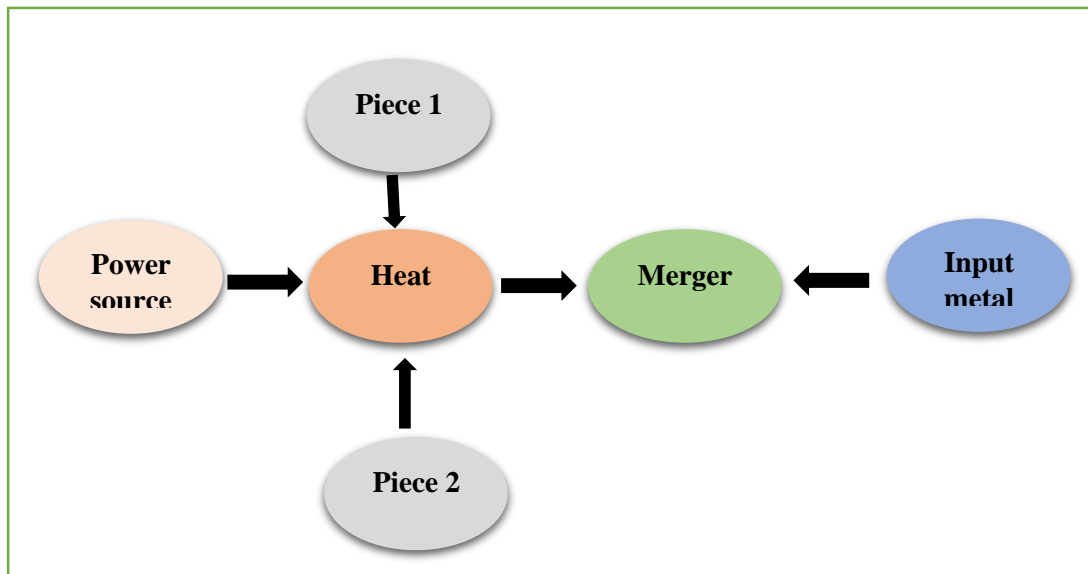
Figure II.1: Schematic of the Welding Process (**M.Hanifa, 2012**)**.**

II.3 Thermal consequences of welding

Regardless of the welding method used to join metal components, four distinct zones are formed, each with unique shapes and characteristics, extending from the original metal structure to the micro-level details in the hardened weld area. These zones include the molten zone, the heat-affected zone, the bonding zone, and the base metal zone, each exhibiting specific mechanical and structural properties, as shown in the following figure (**B.Lotfi, 2018**) (**H.Vahid, 2016**).
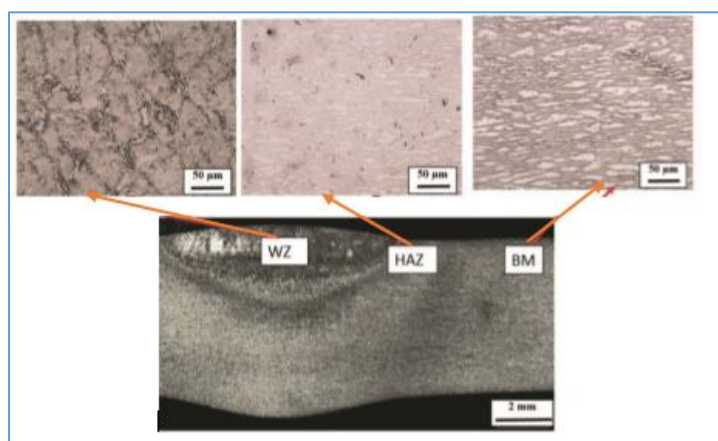
Figure II.2: Typical microstructures observed in welding include the weld zone (WZ), the heat-affected zone (HAZ), and the base metal (BM) of a super duplex stainless steel joint welded using autogenous TIG (Tungsten Inert Gas) welding (**H.Vahid, 2016**).

II.3.1 The weld zone (WZ)

This area is characterized by having reached a liquid state, where concentration gradients can be observed, varying from the hottest region to the cooler parts within the zone **(KH.Farida, 2017).**

II.3.2 The heat affected zone (HAZ)

The heat-affected zone (HAZ) is the region where the temperature ranges between the solidus point and a lower threshold, which is still sufficient to trigger reactions or transformations in the solid state, resulting in structural changes within the base metal **(KH.Farida, 2017).**
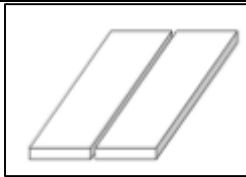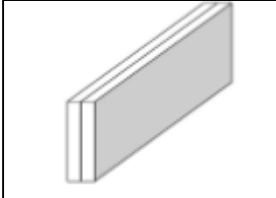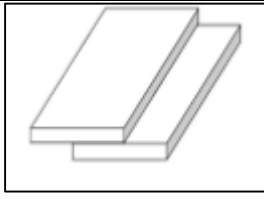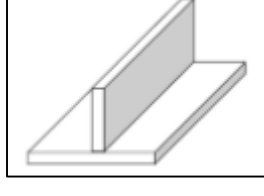
II.3.3 The base metal (MB)

This part of the welded metal structure is positioned far enough from the heat source that it undergoes minimal alterations in its properties during welding. It is situated within the base metal zone **(KH.Farida, 2017) .**

II.4 Type of solder joint

Welds are formed at the intersections of components in a welded structure, which can take on different shapes. There are five primary types of weld joints used for flat materials, as detailed in the following table **(Z.Halim, 2020).**
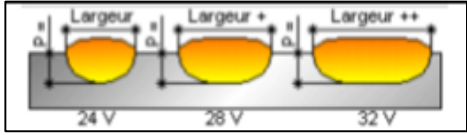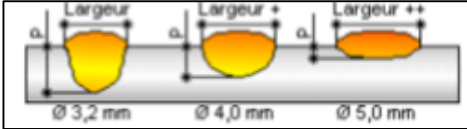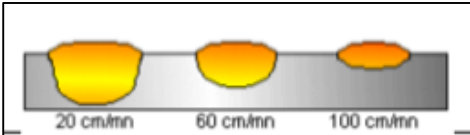
Table II.1: Types of solder joint **(Z.Halim, 2020).**

Types of assembly	Forms
Edge-to-edge assembly: A joint formed between two parts positioned roughly in the same plane.	
Corner Assembly: A joint formed between two parts positioned nearly perpendicular to each other at their edges.	
Edge Assembly: A joint formed between the edges of two parallel parts.	
Clinker assembly: A joint formed between two overlapping parts that are aligned in parallel.	
T-joint: A joint between two flat parts positioned perpendicularly to each other, forming a T-shape.	

II.5 The influence Welding speed

➢ Increased movement speed.

➢ Reduction of penetration.

➢ Reduction of the dimension of the welding bead.

➢ Reduction of the heat emitted (heat input)

➢ The speed of welding affects both penetration and bead geometry. With constant voltage and welding current, increasing the welding speed results in a narrower bead, but it also reduces penetration depth. Higher speeds may cause porosity due to the rapid solidification of molten material, potentially trapping gases. Moreover, welding at very high speeds can lead to the formation of grooves **(B.Ismail, 2017) (M.Younes, 2014).**

Table II.2: The influence of the welding parameters on the welding bead **(M.Younes, 2014).**

If increased values	Width	Penetration	Graphical representation
VOLTAGE	+	=	
INTENSITY	=	+	
Ø THREAD	+	-	
WELDING SPEED	-	-	

II.6. Classification of processes

Various welding processes utilize distinct methods and principles. Some achieve assembly through localized fusion of the materials, while others establish metallic continuity through purely mechanical means without melting. These processes can be effectively categorized based on the types of energy employed **(A.Mouloud, 2003).**
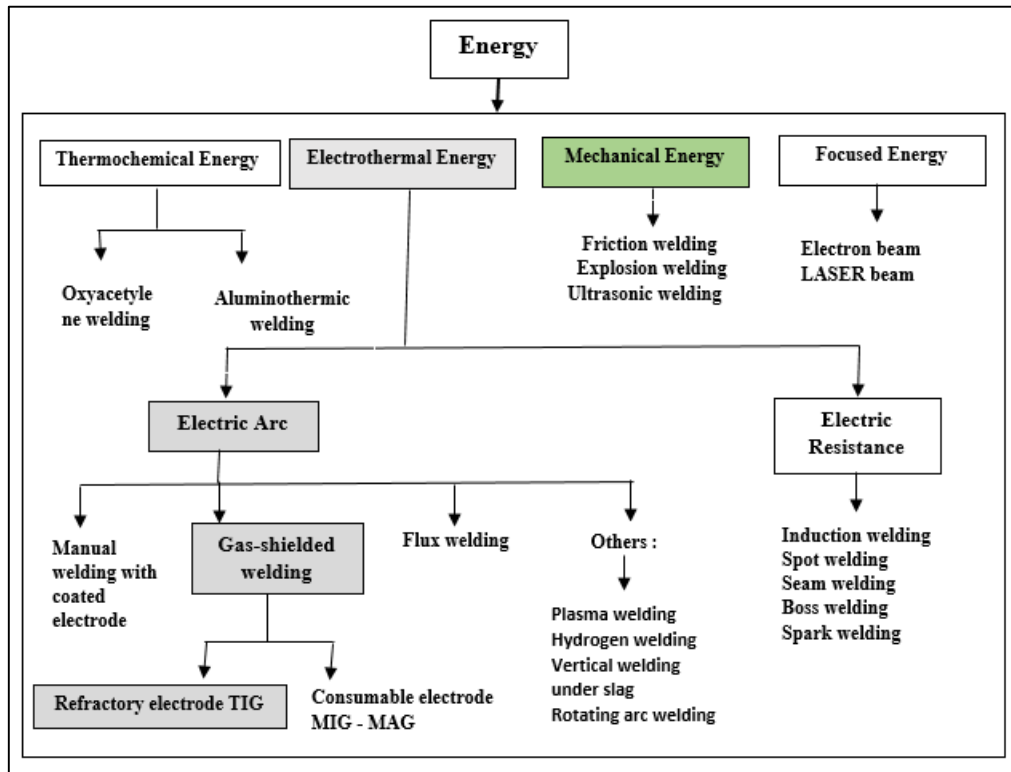
Figure II.3: Classification of welding processes.

This classification allows for a comparison of the energy levels of different sources (Figure II-3). To make the comparison more effective, it is recommended to use the concept of specific energy (energy per unit area). The analysis reveals that electric arc processes have average energy densities, with their efficiency being affected by whether metal transfer takes place. This factor plays a significant role in both arc efficiency and the metal deposition rate, which are key considerations when choosing an appropriate process for a particular application (**B.Hadjer, 2022**).
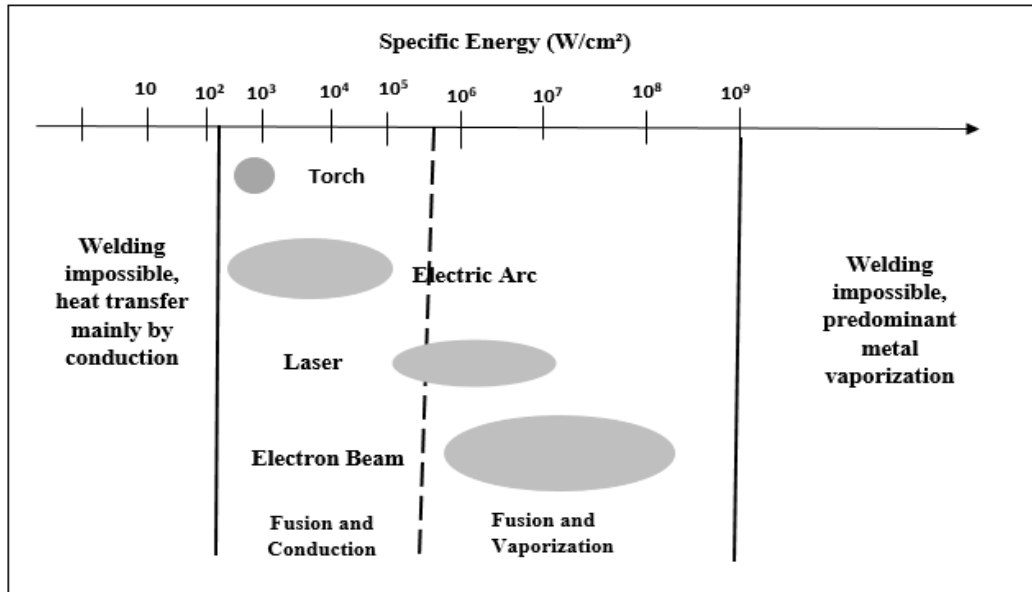
Figure II.4: Comparison of the specific energy of the different processes **(B.Hadjer, 2022).**

II.7 General information on arc welding processes

II.7.1 The main technologies of the arc processes

Arc welding refers to a broad category of welding methods that utilize an electric arc as the heat source for melting and fusing metal materials. This family encompasses four primary processes, each characterized by distinct types of electrodes—such as rods, consumable wires, or refractory electrodes—as well as the type of shielding medium employed, which may include slag or gas to protect against the surrounding atmosphere **(Bachir, 2015).**

II.7.2 Current sources for arc welding

Recent developments in arc welding have brought inverter technology to the forefront as a primary power source. This technology is preferred for its compactness, lightweight design, and ability to support various processes, such as coated electrode, GTAW (Gas Tungsten Arc Welding), and GMAW (Gas Metal Arc Welding). To meet the diverse material requirements, welding station manufacturers have introduced different types of current. Additionally, the growing complexity of metallurgical materials has made improving current resources a crucial challenge in achieving effective weldability **(CH.Julien, 2011).**

II.8 Method Manual arc welding with a coated electrode (SMAW)

II.8.1 Definition

Shielded Metal Arc Welding (SMAW) is one of the most straightforward arc welding techniques. The setup includes a power source, which can be either direct or alternating current, along with an electrode holder, connection cable, and ground cable. Its simple design has made SMAW a fundamental method in the industrial sector since the early 1900s **(KH.Farida, 2017).**

II.8.2 Principle of the process

In this process, an electric arc is established and maintained between the metal core of the electrode and the workpieces being joined. The electrode serves as the filler metal, and the heat generated by the arc melts both the workpieces and the metal core of the electrode, forming a molten pool. The electrode's coating melts shortly after the core, creating a protective gas shield that prevents oxidation of the molten metal due to exposure to air. Once cooled, the weld is covered with slag, which must be removed. This method is mainly used for welding ferrous metals and is versatile enough to be employed in all welding positions **(M.Quentin, 2020).**
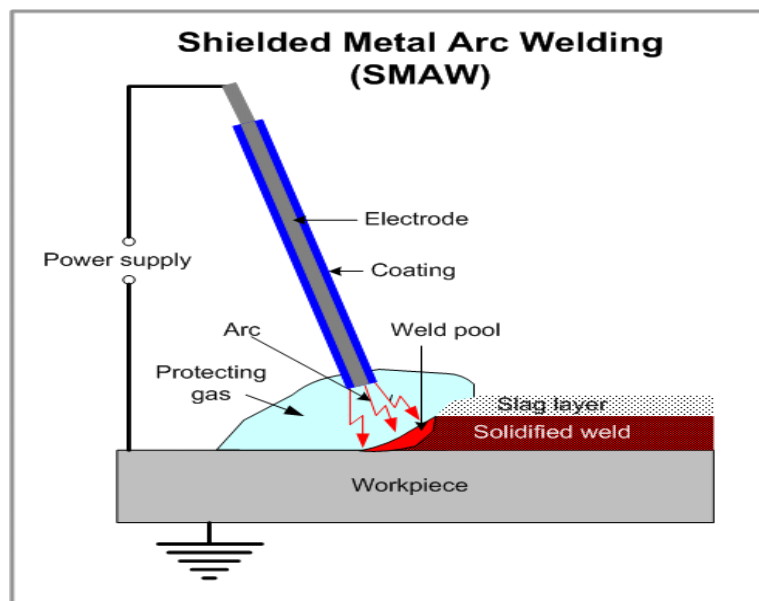
Figure .II.5: Arc welding with SMAW Coated Electrodes: Principle diagram **(Yusof et al., 2020).**

II.9 Definition of the coated electrode

The electrode in Shielded Metal Arc Welding (SMAW) comprises two distinct components:

a) **The Core:** This is the cylindrical metal section located at the center of the electrode. Its primary functions are to conduct the electric current and provide the metal that will be deposited into the weld.

b) **The Coating:** This is the cylindrical outer layer of the electrode. Its primary function is to protect the molten metal from oxidation by creating a shielding gas atmosphere. As the coating melts, it forms a slag over the weld seam, which not only prevents oxidation but also slows down the cooling rate of the molten metal. The coating serves several roles:

➢ The electrical role, ensures the stability and continuity of the arc.

➢ Its metallurgical role, it makes it possible to provide the necessary special chemical addition elements. Its chemical and physical composition is very complex.

Its chemical function is to shield the metal from the effects of ambient air and to slow down the cooling of the weld bead by forming a slag. The diameter of the coated electrode ranges from 1.6 mm to 8 mm, while its total length varies between 250 mm and 500 mm. For specific applications, such as automatic welding, some electrodes can extend up to 1 meter **(B.Hichem, 2013).**

II.9.1 Types of electrode

The electrodes are defined by the diameter of the core and the chemical nature of the coating. The standardized diameters are:

(1,25-1,6-3,15-4-5-6) mm The most commonly used coatings are:

❖ Cellulose coating

❖ The basic coating

❖ The rutile coating **(B.Mostefa, 2012).**
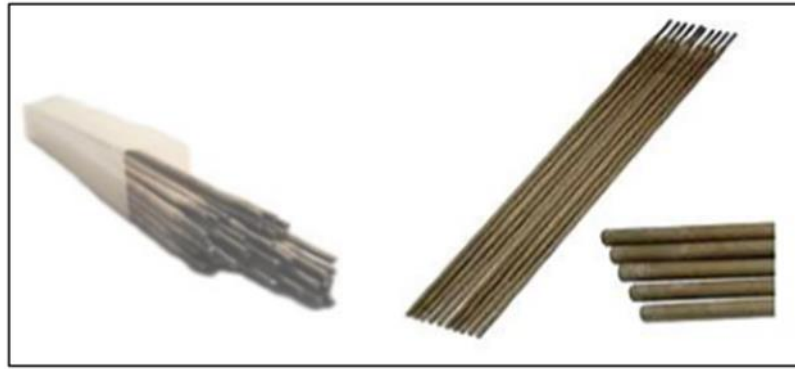
Figure II.7: Welding electrodes **(B.Mostefa, 2012).**

II.10 Applications of SMAW welding

The SMAW welding process is very popular, among other things, in certain specialized tasks such as, for example, pressure vessels and pipes,
 storage tanks, bridges and buildings or ships and wagons. It offers good mobility and the possibility of welding outdoors without special precautions, especially to carry out repairs or work on a construction site **(K.Chaima, 2020).**

II.11 Advantages and disadvantages

II.11.1 Advantages

Coated electrode welding is a widely used method with several advantages:

- **Compact Welding Equipment:** The reduced size of welding machines makes them highly portable and convenient for on-site applications.
- **Versatility:** SMAW can be conducted in any welding position, providing flexibility and allowing for greater independence during the welding process.
- **Cost-Effective:** The equipment required for SMAW is relatively inexpensive.
- **Effective Penetration:** SMAW is capable of achieving good penetration in the weld **(B.Yassine, 2016).**

II.11.2 Disadvantages

- The thermal transmission coefficient of the SMAW process, which indicates the amount of heat transferred to the welded part, ranges from 50% to 85%. This coefficient plays a key role in determining the penetration depth of the weld, allowing SMAW to achieve substantial penetration. However, the concentrated heat at the center of the arc can cause angular deformation in the welded material.

- However, for the initiation of the arc with manual processes (particularly with the electrodes with basic coating for the SMAW), the no-load voltage must be quite high, generally with a minimum value of 70 V **(B.Yassine, 2016).**

Experimental

Part

Chapter III

Materials and methods

III Materials and methods

III.1 Introduction

This chapter concerns the presentation of materials and a sample of **X42** steel welded by the coated electrode arc welding technique **(SMAW)** at the company level national **COSIDER Biskra** pipeline and the various devices implemented for the carrying out experimental analysis tests at the crapc biskra laboratory level and D**CRD / Sonatrach Boumerdès Center for Research and Development**

III.2 Basic metal

The experimental material used in this study is commercially available X42pipeline steel. The chemical composition of this steel includes **(X.Yangz et al., 2018)** is shown in Table I.2 where they are used for hydrocarbon pipelines, welded by the arc welding technique with coated electrode **(SMAW)** with dimensions of **36 ×40 cm** and a thickness **of 1.5 cm** , as shown in **figure III.1**.

Figure III.1: X42 Steel Plate Welded Using SMAW Technique.

III.2.1 Chemical composition of the base metal

It is obtained by spectrometric analysis **(element wave measurement) X42** steel contains a low carbon content **(~0.24%)**.The chemical composition is detailed in **(table I.2).**

III.3 Filler metal

The type of coating Used is the cellulose coating is generally composed of three types of flux varies according to the number of passes as indicated in the following table **(table III.1)**

Table III.1: Types of cellulose flux used during this welding process**.**

Number of passes	types of flows	Daimeter (mm)
1st passe	E 6010	3 mm
2nd passe	E 8010	4 mm
3rd, 4th, 5th passe	E 8010	5 mm

III.3.1 Chemical composition of filler metal

The following table shows the chemical compositions of the flux:

Table III.2: Chemical composition of flux **(Z. idani et al., 2019).**

Flux Mass (%)	Cellulosic Flux: E6010	Cellulosic Flux: E8010-P1
Fe_2O_3	0-90	70-90
MnO	1-5	1-5
SiO_2	---	< 2
Al_2O_3	<5	-----
$C_{18}H_{20}O_6$	<5	<5
TiO_2	<10	<5
$MgCO_3$	<2	<1
$CaCO_3$	---	5-10
CaF_2	---	---
Ni_2O_3	---	<2
CrO_2	-----	----
MoO_3	-----	<1

P1: Specially designated piping electrode

Figure III.2: Coated electrode**.**

III.4 Welding conditions

The welding technique used in this work is coated electrode arc welding **(SMAW)**. The amperage used at the **COSIDER Biskra** welding workshop is **110A**, with a direct or alternating current. We brought two pieces of **X42 steel** of equal dimensions **36 cm** long each piece and we welded them with the **SMAW** welding process and that at different speeds thanks to the change in welding time for each, we finally get two pieces welded at different speeds.

Figure III.3: SMAW welding process**.**

III.5 Experimental methods

The experimental section involved preparing samples at the metallurgy laboratory of the Faculty of Science and Technology at **Mohamed Khider University in Biskra**. This process included cutting the samples with an electric saw, followed by heat treatment to achieve molecular homogeneity. The final step involved polishing the samples.

III.5.1 Samples preparation

The material examined is an X42 steel joint welded using SMAW. To prevent any thermal effects that could lead to structural changes in the samples, the experimental process begins with sample preparation and extends through to structural analysis.

III.5.2 The cutting of the samples

The sample cutting process was carried out in two stages.

- First, the large plates were cut into welded joints containing different welding zones (WZ, HAZ, and MB) using the cold cutting method. This technique prevents heat from affecting the samples by utilizing an aluminum disc with a constant flow of water

Figure III.4: Samples of X42 steel after the welding process Using the SMAW Process**.**

- In the second stage of the cutting process, we used an electric saw using tap water as a lubricant, where we separated the joint areas welded in small pieces each piece representing an area of the welded joint **WZ ,HAZ** and **MB.**

III.5.3 The coating of the samples

The samples, approximately 3 mm thick, were coated to facilitate safe polishing. For this, **Lacoste 813-003** resin, consisting of a transparent liquid and a white powder, was utilized. The procedure involved combining about half a spoonful of the powder with 50 ml of the liquid in a plastic cup and stirring thoroughly with a plastic spoon until a homogeneous, translucent white paste was achieved.

✦ We poured the mixture into plastic molds containing the samples. The samples were left to dry for at least half an hour at room temperature. Afterward, we removed the samples from the molds, making them ready for testing.

III.5.4 Polishing of samples

All samples were carefully polished using abrasive discs of the following grades: **80, 120, 180, 400, 600, 800, 1200, 2400, and 4000**, under a constant flow of water. Additionally, velvet polishing paper and diamond paste were used to remove scratches and further prepare the samples.

III.5.5 The chemical attack

For observations with an optical microscope.

After polishing, we chemically attacked the polished surface with Nital (**al-coolic-nitric solution**) Concentrate **2%** to reveal the microstructures of the different zones of composition :

✦ 2 ml of nitric acid HNO_3.

✦ 98 ml of ethanol C_2H_5OH

- **Mode of operation**

✦ In a gradient test, we measured the volumes of the chemical compositions mentioned above and transferred them into two beakers.

✦ We then mixed these ingredients in a 100 ml volumetric flask.

✦ Using a glass pipette, we extracted a portion of the prepared Nital solution and applied it directly onto the samples. After waiting for a short period, we observed the desired results. Through multiple chemical etching experiments, we determined that **14 seconds** is the optimal time to achieve good results.

✦ Then the samples were washed with distilled Water well.

✦ The samples were dried well by the electric dryer.

With all stages of sample preparation successfully completed, the samples are now ready for microscopic analysis.

III.6 Welding settings

III.6.1 Welding Speed

Welding speed refers to the rate at which the electrode moves along the seam. When the arc voltage stays constant and the speed increases, the weld bead width decreases. There is an optimal speed that maximizes weld penetration; exceeding this speed leads to reduced penetration **(S. Farrukh et al., 2019).**

In this study, the welding speed was determined using the simple arithmetic relationship between distance and time, as expressed by the following equation:

$$\mathbf{S} = \frac{\mathbf{L}}{\mathbf{T}} \qquad \textbf{(III.1)}$$

S : Welding speed (mm/min).

L : represents the length of the welded piece or the length of the weld path (mm).

T : s the time taken to complete the welding over this length (min).

III.6.2 The heat input

The heat input per unit length of the weld is crucial because it affects the cooling rate, which in turn influences the mechanical properties and metallurgical structure of both the heat-affected zone (HAZ) and the weld. This energy or heat input is quantified using mathematical formulas to accurately evaluate its effects **(J. Rohit et al., 2014)(J.Jha et al., 2014).**

$$\mathbf{H} = \frac{\mathbf{60.V.I}}{\mathbf{S}} \qquad \textbf{(III.2)}$$

H : heat input (Kjoule/mm)

V : arc voltage (volts)

I : current (amps)

S : welding speed (mm/min)

III.7 Methods of chemical characterization

To monitor various changes, these samples were analyzed by various material characterization techniques:

+ The Vickers hardness test is the determination of the hardness of the samples.
+ Scanning electron microscopy **(SEM)**, to study surface conditions.

🞣 X-ray diffraction **(XRD)**, for structural characterization, orientation crystalline and determine the average grain.

We present the different techniques that we have used to characterize our materials.

III.7.1 Method of X-ray diffraction analysis (XRD)

III.7.1.1 The principle of X-ray diffraction

The principle of X-ray diffraction involves irradiating a sample with a monochromatic X-ray beam. The scattered waves are collected effectively when they meet the Bragg condition, which dictates...

$$2d(hkl). \, Sin\theta = n\lambda \qquad \textbf{(III.3)}$$

Knowing **λ** and **θ, d(hkl**) is determined. By comparison with the database of **JCPDS** files, the analyzed structures can be identified. The exploitation of the results was carried out using the Philips X'VERT Graphics software **(K.Noureddine, 2007).**

III.7.1.2 Parameters of XRD

a) Crystal size

X-ray diffraction peak profile analysis is a powerful method for studying the microstructures of crystalline materials. The broadening of diffraction peaks indicates the presence of small crystallites or lattice defects in the material. This broadening can be analyzed based on its specific dependence on diffraction order. Crystal size, determined through X-ray diffraction, plays a crucial role in the physical properties of nanomaterials. Precise control over crystal size is necessary for tailoring materials to achieve specific properties. Several methods, including direct observation using scanning electron microscopy **(SEM)**, are commonly used to estimate crystal size. In this study, crystal size values **(denoted as D)** were determined using X-ray diffraction and the X'pert HighScore Plus software. This approach, supported by equation III.4, provides a reliable method for evaluating crystal size, offering essential insights for the precise fabrication of materials with desired characteristics **(V. Uvarov et al., 2007) (W. Sutapa et al., 2018) (T. UngaÂr et al., 2001).**

$$\textbf{D} = \frac{K\lambda}{\beta cos \, \theta} \qquad \textbf{(III.4)}$$

K: is Debye – Scherer's constant (0.94).

λ : is the wavelength of the CuKα radiation (0.154 nm).

B : is the full width half maximum **(FWHM)** of the peak.

θ : is the Bragg's angle samples.

b) Dislocation density

Dislocations are linear defects in crystalline materials that disrupt the regular arrangement of atoms within the crystal lattice. Dislocation density, a key factor in materials like metals and crystalline ceramics, quantifies the concentration of these dislocations. Represented by δ, dislocation density measures the number of dislocation lines per unit volume of the crystal, reflecting the degree of crystal imperfections. Dislocation density is typically calculated using equation III.5. This measurement is important as it provides valuable insights into the crystallinity of nanoparticles, offering information about the material's crystalline quality and its potential mechanical properties and structural integrity **(W. Sutapa et al., 2018)(T. UngaÂr et al., 2001).**

$$\delta = \frac{1}{D2} \qquad \textbf{(III.5)}$$

c) Preferred orientation

The preferred orientation can be detected through quantitative analysis using specific software or by using pole figures, which is an optical tool that shows the distribution of the crystalline orientation within a sample. In this work, we determined it by calculating the texture coefficient **(TC)**, a measure used in X-ray diffraction **(XRD)** analysis to identify the preferred orientation of crystals in a material. To calculate it, we used the following formula:

$$\textbf{TC}_{\textbf{(hkl)}} = \frac{\frac{I(hkl)}{I0(hkl)}}{\frac{1}{N}\sum_{i=1}^{N}\frac{I(hkl)}{I0(hkl)}} \qquad \textbf{(III.6)}$$

TC(hkl) : Texture coefficient.

I(hkl) : Measured intensity of a specific crystallographic plane **(hkl)** in the sample.

I0(hkl): Intensity of the same plane in a reference sample with random orientation.

N: Number of reflections **(planes)** considered in the analysis.

If:

- **TC > 1:** Indicates that the crystallographic plane **(hkl)** is more aligned or favored in the sample.

- **TC < 1:** Suggests that the plane is less aligned or underrepresented in the sample.

- **TC = 1:** Implies that the plane's orientation is comparable to that of a randomly oriented sample **(S. Chakrabarti et al., 2004)(M. Birkholz et al., 2007)(M.Majeed et al., 2013)(C.**

Atilla and al., 2004)(W. Yaqin and al., 2015)(M. Rashidi and al., 2011)(S. Rafael and al., 2019) .

III.7.1.3 Method of operation

At this stage of sample preparation for X-ray diffraction **(XRD)** analysis, we utilized the cut and polished samples directly, without any chemical treatment or coating. For the analysis, we used a **Bruker D8** Advance diffractometer, operating within an angular range of 10° to 100° on the 2θ scale. **The D8 Advance**, part of the D8 series of diffractometers, is designed to accommodate a wide range of diffraction applications.

Figure III.5: Diffractometer BRUKER D8 ADVANCE.

III.7.2 Hardness tests

III.7.2.1 Vikers hardness test (Hv)

a) **The vikers hardness test principle**

Hardness is a material property that reflects its resistance to deformation or localized penetration. The hardness testing procedure involves applying a force to an indenter, which then penetrates the material. The indenter is held in place for a set period, and once removed, the indentation left on the surface is measured. The Vickers hardness test, introduced in 1925 by engineers at the English company Vickers, revolutionized hardness testing by allowing very low forces to be applied and enabling measurements on thin films. The test uses a diamond indenter with a pyramidal shape and a square base, with the angle between opposite faces at the apex being 136°. Since the indentation is usually small, optical microscopy is used to measure its diagonals to determine the hardness of the sample **(L.Xiongjie, 2013).**

a) **Method of operation**

In this work, we tested the Vickers hardness using a FALCON 600 brand device

Figure III.16: Falcon 600 device used to test Vickers hardness.

❖ After a good polishing of the samples and the chemical attack process.We have fixed the samples well inside the dedicated sample holder in the machine.

❖ A known force is applied for a specific duration by pressing an indenter (cone or sphere) into the surface of the material being tested.

❖ Then We used the Vickers hardness test where we determined the 10Hv hardness scale, then we started the test The test took at least 10 seconds for each point We finally got at least 30 points for each sample.
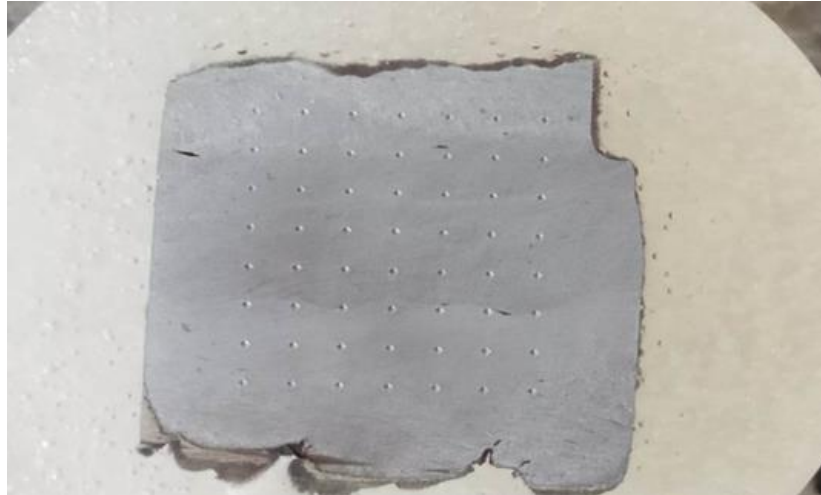
Figure III.7: The Shape of the sample after the Vickers hardness test.

III.7.2.2 Brinell hardness

   The Brinell hardness principle

   The Brinell method is widely used to evaluate the hardness of heat-treated steel, especially those with unpolished surfaces. In this technique, a solid steel ball is used as the indenter, and the hardness is determined by measuring the diameter of the indentation (d) left on the surface after the load is removed. This diameter is then compared to specific tables outlined in **GOST 9012-59 (Measure 5)**. The basic principle of the Brinell hardness test can be summarized as follows:

HB represents the measured value of Brinell hardness.

$$\text{HB}= 0.102.2\text{F}/\ \pi\ \text{d. (D-}\sqrt{D^2 + d^2}) \qquad \textbf{(III.7)}$$

The previous equation is used after conducting the Brinell hardness test.

The hardness values for Vickers and Brinell can be related using the formula:

$$\textbf{HB = 0.95 HV} \qquad \textbf{(III.8)}$$

Which is particularly valid for annealed materials. This relationship was applied in this work to estimate the hardness (HB) **(G. Leyi et al., 2011)(G. Sandomirskii et al., 2017).**

III.7.2.2 Parameters of hardness tests

Ultimate strength σut and yield strength σy

Absolute strength and yield strength are critical mechanical properties that define a material's capacity to resist deformation and failure. Absolute strength is the maximum stress a material can endure before fracturing, whereas yield strength marks the point at which the material starts to undergo permanent deformation. To calculate both yield strength and ultimate strength, two methods can be used based on hardness values, specifically utilizing the Vickers hardness **(Hv)** scale and the Brinell hardness **(HB)** scale **(M. Mostafavi et al.,2015)(G.Pasqualino et al., 2018).**

$$\sigma ut = 2{,}4079.Hv + 46{,}39 \qquad \text{(III.9)}$$
$$\sigma y = 2{,}9263.Hv - 44{,}289 \qquad \text{(III.10)}$$
$$\sigma ut = 0.0012.HB2 + 3.3.HB \qquad \text{(III.11)}$$
$$\sigma y = 0.0039.HB2 + 1.62.HB \qquad \text{(III.12)}$$

III.7.3 Scanning electron microscopy (SEM)

a) The principle

Scanning Electron Microscopy (SEM) is a technique used to examine surface topography. It provides detailed information about a sample's structure and texture, as well as the size and shape of its constituent grains or agglomerates, depending on the selected magnification. The method involves detecting secondary electrons that are emitted from the surface when a focused beam of monokinetic primary electrons interacts with the sample. This interaction occurs in a region known as the interaction volume, which is detected by a sensor. The sensor controls the brightness of a cathode oscilloscope, with the scanning process synchronized with the movement of the electron beam **(S.Mounir, 2017).**

b) **Method of operation**

This characterization process utilized a Quantum 650 scanning electron microscope (SEM) combined with energy dispersive X-ray spectroscopy (EDX). This approach enabled the analysis of material compositions and allowed for an examination of how welding speed influences these characteristics.
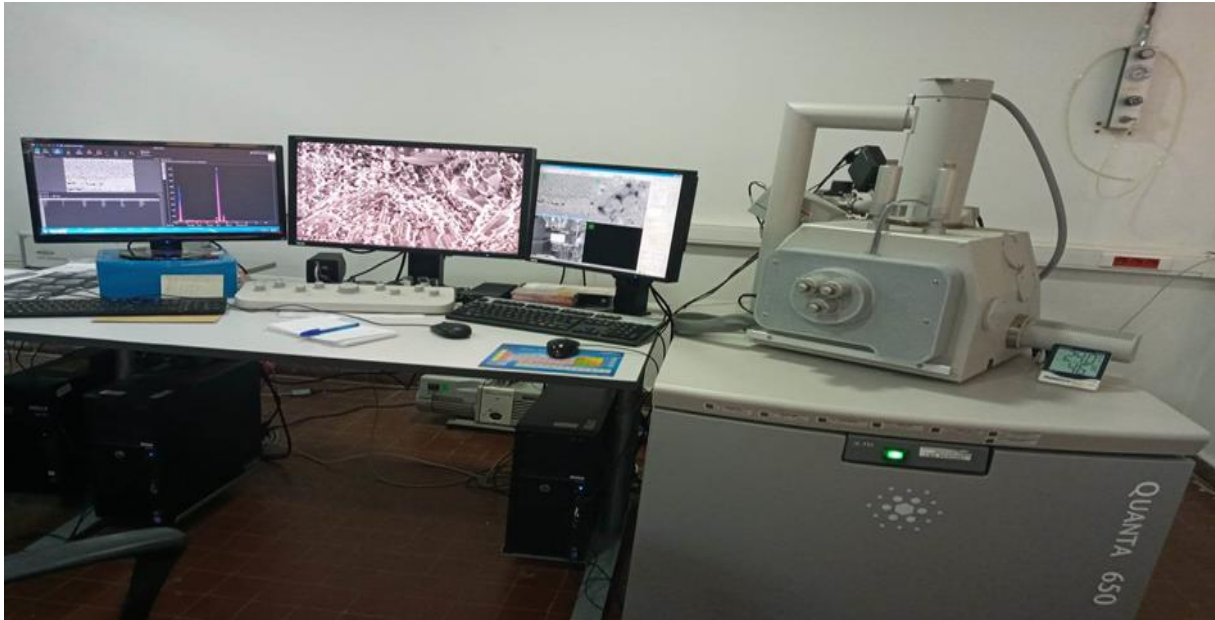
Figure III.8: Scanning Electron Microscopy (SEM) Equipment.

➢ This test was carried out after a good polishing of the samples and the chemical attack process.

➢ Fixing the samples on the special sample holder.

➢ Cleaning the surface of the impurity samples with nitrogen gas.

➢ The samples are placed in order in the place designated for them inside vacuum chamber.

➢ This process takes from 30 minutes to 45 minutes each to achieve results.

Chapter IV

Results and Discussion

IV Discussion of results

IV.1 Introduction

This chapter presents the experimental results obtained through various characterization techniques, including X-ray diffraction (XRD), Vickers hardness testing (HV), and scanning electron microscopy (SEM), for all regions of the welded joint (base metal MP, heat-affected zone HAZ, and weld zone WZ).

It includes the results of the study on the effect of welding speed using Shielded Metal Arc Welding (SMAW) on the properties of X42 steel. A similar study was also conducted on X70 steel in order to compare the structural and hardness behavior of both types of steel. The data were processed using several software tools: Origin for data analysis and graphing, Highscore for crystal structure analysis, Match 4 for advanced X-ray data interpretation, and Mountains Software for analyzing and processing both crystal and microscopic images. Additionally, Python 3 was used to create accurate graphs.

IV.2 Calculation of welding settings

In this study, we employed the **SMAW** welding process with a cellulose electrode to weld **X70 steel** at two distinct speeds. The parameters of the welding process are outlined in the following **table I.V.1**:

Table .IV.1: SMAW welding settings**.**

speed	Number of passes	I welding currents A	U Tension électrique V	S The welding speed (mm/min)
S_1	5	110 A	80 V	20
S_2	5	110 A	80 V	35

IV.2.1 Analysis and Interpretation of the heat input

❖ **Analysis of results**

Using the mathematical relationship (III.2), we derived two values for the input heat, as presented in **Table 2**. For the first speed, $S_1 = 20$ **mm/min,** the input heat was calculated as **H₁**

= **26.4 kJ/mm**. In contrast, at the second speed, $S_2 = 35$ mm/min, the input heat was $H_2 = 15.08$ **kJ/mm**. This shows that the slower speed resulted in a higher input heat compared to the faster speed**.**

❖ **Interpretation of results**

The results reveal that lower welding speeds allow the electric arc to remain stationary for a longer period, thereby increasing the heat input to the metal. In contrast, higher speeds cause the electric arc to move more quickly, reducing the time spent on each area and subsequently decreasing the heat input (**A. Ravisankar et al., 2014**). A greater heat input generally leads to smaller defect sizes and lowers the risk of crack formation in the weld, which typically improves welding quality (**N. Jerzy et al., 2005**) at this initial speed. On the other hand, reduced heat input is associated with enhanced strength and elasticity, due to the formation of smaller crystal sizes in the welds produced at the higher speed (**S. Kumar et al., 2011**). Moreover, heat input has a significant effect on cooling rates; higher input slows cooling, potentially decreasing hardness, while lower input accelerates cooling, which may increase hardness but also introduce defects. Therefore, the interplay between heat input and cooling rates has vital implications for the microstructure and mechanical properties of the weld. (**W. Bo etal., 2017**)**.**

❖ **Conclusion**

In conclusion, welding speed plays a crucial role in determining heat input, which directly affects the weld's quality and properties. Slower welding speeds result in higher heat input, which helps reduce defects such as cracks and improves weld quality. However, the increased heat can lead to a reduction in hardness due to slower cooling rates. On the other hand, faster welding speeds lower heat input, enhancing hardness and strength due to quicker cooling. However, this faster cooling can cause defects, which may compromise the overall quality of the weld.

IV.3. Analysis and Interpretation of X-ray diffraction (XRD) results

Figure IV.1 shows the comparison of the X-ray diffraction spectra of the three zones of the welded **steel joint X 70** at two different speeds, according to international sheets (**Table IV.1**), the results obtained were processed using a program **x'pert highscore plus** it is a comprehensive instrument that combines crystallographic analysis and phase identification. Where we get good and accurate results using it as described below:
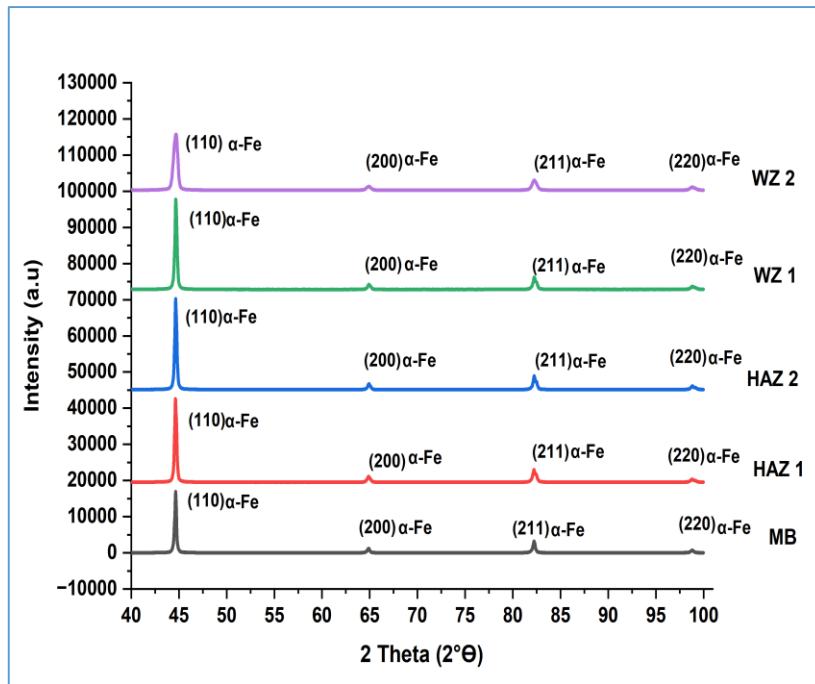
Figure IV. 1: Comparison of X-ray diffraction XRD patterns of different welding zones for the two speeds (HAZ1,HAZ2,WZ1,WZ2 and MB)**.**
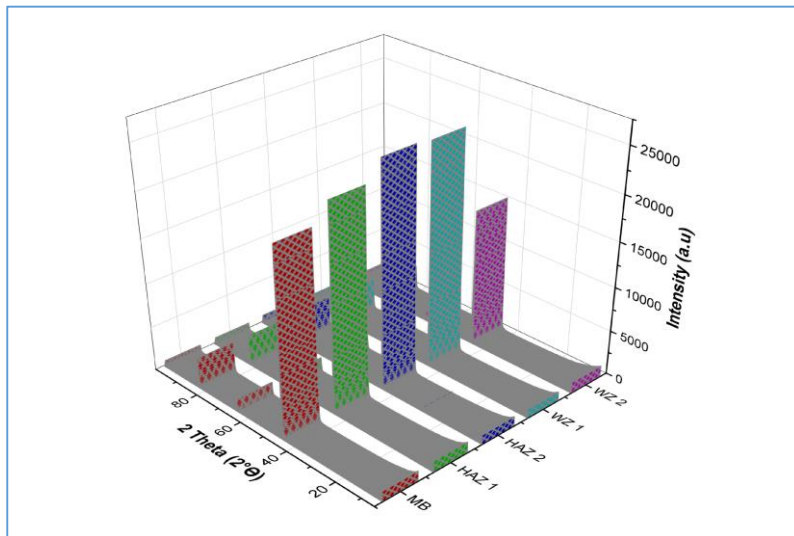
Figure IV.2: Comparison of X-ray diffraction XRD patterns of different welding zones for the two speeds (HAZ1,HAZ2,WZ1,WZ2 and MB) 3D.

Table .IV.2: The results of the analysis of X-ray diffraction spectra of different welding zones (HAZ$_1$,HAZ$_2$,WZ$_1$,WZ$_2$ and MB) for the two speeds using the X-Bert highscore Plus program.

Peaks	Pos. [°2θ.]	FWHM Left [°2Th.]	HKL)miller index	D Crystals siz [nm]	σ Dislocation density *10^-3 (nm^-2)	degree of crystallinity %
MB						
1	44,64	0,24249	110	55 .5	0.32	85
2	64,89	667,23258	200	36	0.77	
3	82,12	0,33109	211	46.8	0.45	
4	98,69	0,35721	220	26.4	1.43	
HAZ$_1$						
1	44,62072	0,21522	110	59.6	0.28	72
2	64,84881	0,31095	200	34.7	0.83	
3	82,19963	0,33172	211	42.7	0.54	
4	98,77371	0,35339	220	30.8	1.05	
HAZ$_2$						
1	44,60686	0,23616	110	59.3	0.28	65
2	64,84354	0,17712	200	37.6	0.71	
3	82,2365	0,18	211	51.2	0.38	
4	98,80326	0,32152	220	30.8	1.05	
WZ$_1$						
1	44,6527	0,22214	110	60.3	0.27	84
2	64,89216	0,29621	200	31	1.04	
3	82,23141	0,31592	211	44.9	0.49	
4	98,81068	0,216	220	27.1	1.36	
WZ$_2$						
1	44,61623	0,49604	110	21.8	2.1	73
2	64,84591	0,46182	200	19.8	2.5	
3	82,19114	0,48527	211	26.8	1.39	
4	98,75531	0,45833	220	26.4	1.43	

The analysis of the X-ray diffraction spectrum reveals consistent peaks across the welding zones **(WZ, HAZ, and MB)** for both welding speeds, although variations in intensity are observed. Additionally, there are differences in the number and diameter of crystals between the welding zones corresponding to the first and second speeds, as indicated in the results presented in the previous table.

The consistent peaks suggest that the matrix of X70 steel remains stable with a centered cubic structure, confirming the absence of impurities. Intensity variations indicate a preferred orientation, and differences in crystal quantity and size emphasize the heat effect from the base metal during welding**.**

❖ **Analysis of results**

First speed S_1 (HAZ$_1$, WZ$_1$ and MB)

At a speed of **S_1 = 20 mm/min**, the analysis of the X-ray diffraction spectrum reveals that the welding zones **(WZ$_1$, HAZ$_1$, MB)** exhibit identical diffraction patterns, although the intensities differ. The **110 peak** in the **WZ$_1$** zone is notably the most prominent among all peaks. Additionally, there are clear differences in both the quantity and size of crystals in these zones. The distribution of peak density closely aligns with the Iron phase peaks found in the Joint Commission's powder diffraction standards database for base metals **(MB)**, with only minor variations in the Bragg angles **(2 Theta)** and peak densities in other**.**

Second speed S_2 (HAZ$_2$, WZ$_2$ and MB)

At a speed of **S_2 = 35 mm/min**, analysis of the X-ray diffraction spectrum indicates that the welding zones **(WZ$_2$, HAZ$_2$, MB)** display identical peaks, though there are noticeable differences in their intensities. The **110 peak** in the **WZ$_2$** welding zone is particularly prominent, emerging as the highest among all peaks, which suggests a variation in crystal density distribution. While the peak density distribution is similar to that of the Iron phase in the base metal **(MB)**, there are significant differences in the Bragg angles **(2 Theta)** and peak densities in the other welding zones. This variation highlights the impact of welding speed on the crystal structure across the different zones**.**

❖ **Interpretation of results**

The appearance of the same four peaks across all regions **(MB, HAZ, WZ)** for both welding speeds in **X70 steel** indicates that the material's crystal structure, specifically the face-centered cubic **(FCC)** structure of iron, remains consistent. This stability in peak positions suggests that the welding process did not alter the core crystalline matrix, preserving the steel's original properties. Moreover, the uniformity of these peaks across samples confirms that no impurities were introduced during welding, which is essential for maintaining material integrity.

A significant increase in peak intensity on the **(110) plane**, especially in the **WZ₂** welding zone, suggests crystallization effects that enhance ductility. This is reinforced by the presence of a supersaturated α-phase iron **(ferrite)**, which indicates effective solidification during welding and contributes to the toughness and ductility of the welded joint. This **α-phase** ferrite plays a crucial role in providing the welded steel with the necessary balance of strength and flexibility, important for structural applications. Additionally, the consistent peak positions across different regions indicate minimal residual stress or distortion, further underscoring the stability of the crystal structure. Minor variations in peak intensity, particularly in the **(110) plane**, may relate to localized shifts in grain orientation and crystallographic texture resulting from the welding process, aligning with observed mechanical properties. The slight shifts in **(2θ)** angles reflect differences in spacing between crystal planes **(hkl)**, and minor changes in these angles across samples could indicate internal stresses or structural adjustments due to the welding **(CH.Nedjema, 2015), (K.Nitin et al., 2021), (N. JiaF et al., 2017) (S.Aqida et al., 2013)(W. Sowards et al., 2008)(B. Maalache et al., 2018).**

❖ **Conclusion**

The analysis indicates that welding speed has a notable impact on the crystal structure of **X70 steel**. Lower welding speeds promote stability in the crystal structure, resulting in larger and more stable crystals that enhance weld quality and peak density. Conversely, higher speeds alter crystal distribution, potentially reducing ductility and introducing defects due to rapid cooling. In summary, slower welding speeds improve crystal structure, while faster speeds may compromise weld quality and increase internal stresses**.**

IV.3.2 Analysis and Interpretation of dislocation density and crystal size results
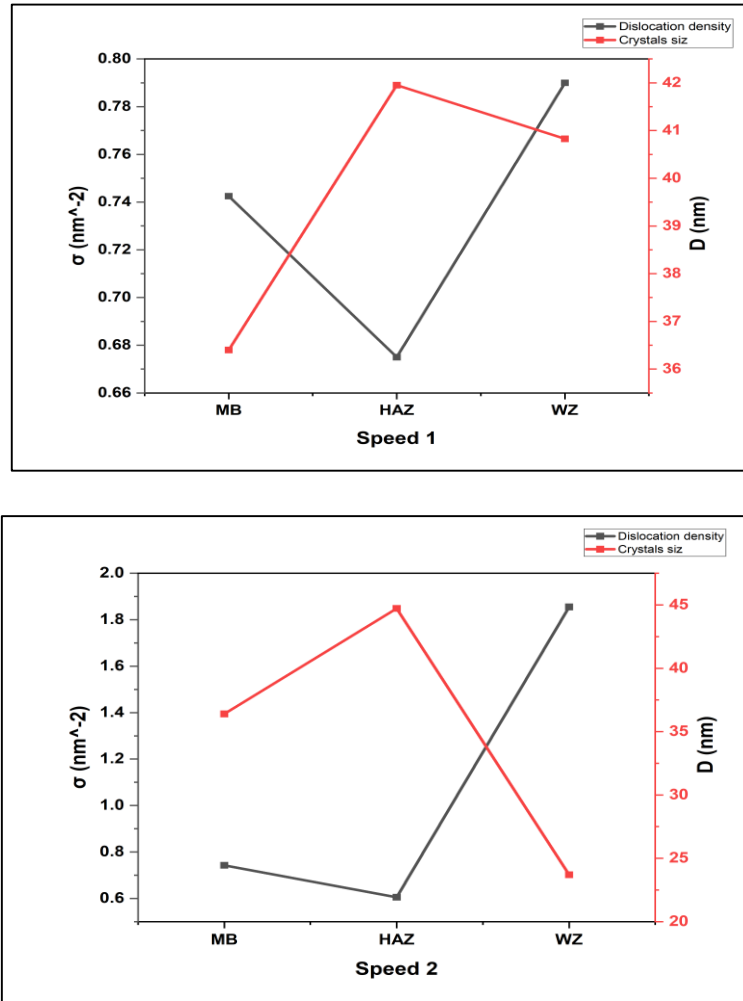
Figure IV.3: Comparison Curves of dislocation density and crystal size in different weld zones at two welding speeds of steel X70**.**

Based on the results in Table IV.2 and the curves in Figure IV.3, the dislocation density and crystal size can be analyzed and interpreted as follows:

❖ **Analysis of results**

This analysis evaluated the crystal size and dislocation density across different zones produced by welding at two distinct speeds. The results were structured into two primary sections:

✚ Crystal size

First speed (HAZ$_1$, WZ$_1$ and MB)

At the first welding speed, the zones show comparatively larger crystal sizes. In **HAZ$_1$**, the crystal size varies from **30.8 nm to 59.6 nm**, while in **WZ$_1$**, it ranges between **27.1 nm** and **60.3 nm**, suggesting that this speed supported enhanced crystal growth during cooling**.**

Second speed (HAZ2, WZ2 and MB)

At the second speed, especially in **WZ$_2$**, a significant reduction in crystal size is observed, ranging from **19.8 nm to 26.8 nm**. This implies that the increased welding speed led to quicker cooling, which limited crystal growth, resulting in smaller crystals compared to those formed at the first speed**.**

✚ Dislocation density

Dislocations are imperfections within the crystal structure that lead to permanent plastic deformations in crystalline materials, such as metals. These dislocations vary with the material and play a key role in determining many of its mechanical properties **(D.Arnaud et al., 2019).**

First speed (HAZ$_1$, WZ$_1$ and MB)

At the first speed, **HAZ$_1$** and **WZ$_1$** show relatively low dislocation density compared to the second speed, with values between **0.28** and **1.36 nm^{-2}**. These results indicate fewer deformations and moderate thermal stresses**.**

Second speed (HAZ$_2$, WZ$_2$ and MB)

At the second speed, a significant increase in dislocation density is observed, especially in **WZ$_2$**, where it reaches **2.5 nm^{-2}**. This considerable rise in dislocation density indicates a higher level of deformations resulting from rapid cooling, which contributes to a greater number of crystal defects and suggests increased thermal stresses**.**

❖ Interpretation of results

The first, slower welding speed promoted larger crystal growth and resulted in fewer deformations within the material, fostering a stable crystal structure with reduced residual stresses. In contrast, the faster second speed led to quicker cooling, resulting in smaller crystal sizes and increased yield strength. However, this rapid cooling may also raise residual stresses within the material, potentially negatively impacting its mechanical properties **(T. Shintani et al., 2011)(W. Li et al., 2020)(M.Sablik et al. , 2001).**

❖ **Conclusion**
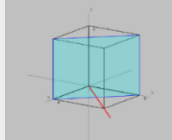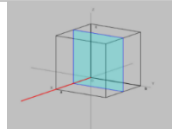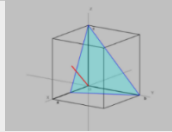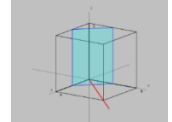
The results analysis reveals that welding speed has a significant effect on both crystal structure and dislocation density. A lower speed **(S_1 = 20 mm/min)** leads to improved crystal size and stability, while a higher speed **(S_2 = 35 mm/min)** may result in greater material deformation due to rapid cooling. This indicates an inverse relationship between dislocation density and crystal size: as crystal size increases, dislocation density decreases, and conversely**.**

IV.3.3 Analysis and interpretation of miller index hkl results

The table below indicates the orientation of the crystal planes using Miller indices. These results were obtained from a website created by **Jean-Jacques Rousseau**, a professor of physics in social sciences at **the French University of Maine (Le Mans) (A.safa and al., 2024).**

The table shows that across all welding zones and at both speeds, the majority of the crystals are oriented along the primary direction of **hkl = 110.**

Table IV.3: Identification the direction of the crystal planes in Miller Index hkl of steel X70.

Miller Index hkl	Miller
110	
200	
211	
220	

Based on the results in **Table IV.3**, which illustrates the orientation of the crystal planes in **X70 steel** welded using the **SMAW** technique, it is clear that four specific crystal planes were consistently observed across all samples. By correlating these results with previous findings, we can analyze and interpret the outcomes as follows**.**

❖ **Analysis of results**

These planes reflect different crystallographic orientations within the structure of **X70 steel,** which play a crucial role in determining mechanical properties such as hardness and durability. To gain a deeper understanding of their effects, we will analyze each of the four planes individually.

- **Plane 110:** This indicator represents the orientation of the crystal plane along the a-b axes, while not intersecting the c axis. Generally, this plane is perpendicular to the c axis within the crystal structure.

- **Plane 200:** The **200** indicator denotes a plane that is perpendicular to the a axis and intersects the **b and c axes**. The figure illustrates the crystal plane symmetrically centered on the **b and c axes**.

- **Plane 211:** At this level, the figure shows increased complexity in the distribution of crystals along these axes.

- **Plane 220:** This indicator intersects equally with the **a-b axes** but does not intersect with the **c axis**. Thus, it represents a plane defined solely by the a-b axes**.**

❖ **Interpretation of results**

The four crystal planes demonstrate unique mechanical properties influenced by their orientation and stress distribution.

The **110 plane** is recognized for its durability and structural stability due to its stress distribution along the **a-b axes**, making it ideal for applications that require high stability in horizontal directions. T

he **200 plane** offers good rigidity and stability in vertical orientations, which is beneficial for applications that demand resistance to vertical stresses.

The **211 plane** improves overall durability by distributing stresses across three directions, making it suitable for dynamic or alternating loads.

Finally, the **220 plane** effectively resists stresses in the **a-b plane**, providing moderate stability and resistance to horizontal loads, making it well-suited for applications that require a balance between rigidity and durability **(M. Mohammad et al., 2017)(M. Mohammad et al., 2015)(Das Bakshi et al., 2019)(CH.Soumya et al., 2017) (A.safa et al., 2024).**

❖ **Conclusion**

The analysis and interpretation of the results reveal that the four crystal planes identified in the X70 steel structure play a crucial role in determining the material's mechanical properties.

The varying orientations of these crystal planes significantly affect stress distribution, which consequently influences the overall performance of the steel.

IV.3.4 Analysis and interpretation of degree of crystallinity results

Crystallinity refers to the regularity of a material's crystalline structure, indicating the proportion of crystalline to amorphous regions. A high level of crystallinity signifies a well-ordered internal structure, which improves mechanical properties like strength. In contrast, low crystallinity indicates disorder within the material, potentially weakening its performance. Techniques such as X-ray diffraction (XRD) are commonly used to assess a material's crystallinity **(B.Luis et al., 2011)(G. Chukhchin et al., 2016).**

In this study, crystallinity was determined by analyzing the X-ray diffraction (XRD) spectra with the X'Pert HighScore Plus software, in combination with Origin software for data analysis. This method enabled precise identification of crystalline phases and the calculation of crystallinity by evaluating the intensity and area of diffraction peaks. By using these software tools together, we were able to accurately quantify the crystalline and amorphous components of the samples, providing a thorough understanding of their structural properties.

❖ **Analysis of results**

First Speed (HAZ$_1$, WZ$_1$, MB)

At this welding speed, the base metal **(MB)** retains a high crystallinity of 85%, indicating that its original crystal structure remains mostly intact throughout the welding process. In the heat-affected zone **(HAZ$_1$)**, the crystallinity decreases to 72% as a result of heat exposure, leading to partial recrystallization and some distortion of the structure. In the weld zone **(WZ$_1$)**, the crystallinity increases to 84%, which is nearly identical to the base metal. This suggests that the gradual cooling process allowed the crystals to reorganize effectively, maintaining a relatively stable structure. orderly crystal structure.

Second Speed (HAZ$_2$, WZ$_2$, MB)

At the higher welding speed, the base metal **(MB)** maintains a crystallinity of 85%, similar to the first speed, indicating that the base metal's structure remains largely unchanged by the welding process. In the heat-affected zone **(HAZ$_2$)**, the crystallinity decreases significantly to 65%, suggesting that the faster cooling rate associated with this speed introduced more distortions in the crystal structure. In the weld zone **(WZ$_2$)**, the crystallinity is measured at 73%,

which is notably lower than that observed in the first speed's weld zone. This reduction reflects the effect of rapid cooling, which disrupts the crystal structure's orderly arrangement, leading to decreased stability.

❖ **Interpretation of results**

At the slower speed **(S_1 = 5 mm/min)**, the gradual cooling process preserved a high degree of crystallinity in both the weld zone **(WZ_1)** and the heat-affected zone **(HAZ_1)**. This suggests the formation of a more stable crystalline structure, which contributes to the enhancement of the material's mechanical properties **(T. Atsushi et al., 2015)**.

In contrast, the heat-affected zone showed a slight reduction in crystallinity, indicating partial recrystallization resulting from the heat exposure during the welding process **(V. Kolubaev et al., 2020).**

At the higher speed **(S_2 = 35 mm/min)**, rapid cooling resulted in a reduction in crystallinity in both regions. The crystalline structure in the weld zone **(WZ_2)** was less uniform, indicating greater distortions due to the limited time for atomic rearrangement. Furthermore, the heat-affected zone **(HAZ_2)** experienced a more pronounced decrease in crystallinity compared to the slower speed, suggesting that higher welding speeds can lead to a less stable and mechanically weaker structure **(E. Curiel-Reyna et al., 2006) (R. Eslam etal., 2012).**

This highlights how different welding speeds can impact the crystallinity properties in various regions of the weld **(A.Herrera et al., 2005).**

❖ **Conclusion**

The results indicate that welding speed significantly affects the crystallinity properties across different regions of the weld. Slower speeds, with their gradual cooling, promote the formation of a stable crystalline structure, thereby improving mechanical properties. Conversely, higher speeds cause rapid cooling, which reduces crystallinity and leads to greater distortions, resulting in a less stable structure. Therefore, controlling welding speed is essential for optimizing material performance, emphasizing the need to study how varying speeds influence crystallinity and overall material characteristics.

IV.3.5 Analysis and Interpretation of preferred orientation results

Using the **Match 4** program for X-ray diffraction analysis and the mathematical relationships outlined previously, we obtained the results summarized in **Table IV.4**. **Python 3** was employed to generate a color map, illustrated in **Figure IV.4**, as well as a polar plot displaying the distribution of the texture coefficient in the samples, shown in **Figure IV.5**.

Table IV.4: Texture coefficient (TC) values for different peaks in various samples**.**

Samples	TC (peak 1)	TC (peak 2)	TC (peak 3)	TC (peak 4)
MB	3.15	0.21	0.52	0.12
HAZ$_1$	3.22	0.21	0.46	0.11
WZ$_1$	3.3	0.18	0.43	0.11
HAZ$_2$	3.2	0.2	0.46	0.13
WZ$_2$	3.1	0.2	0.54	0.16

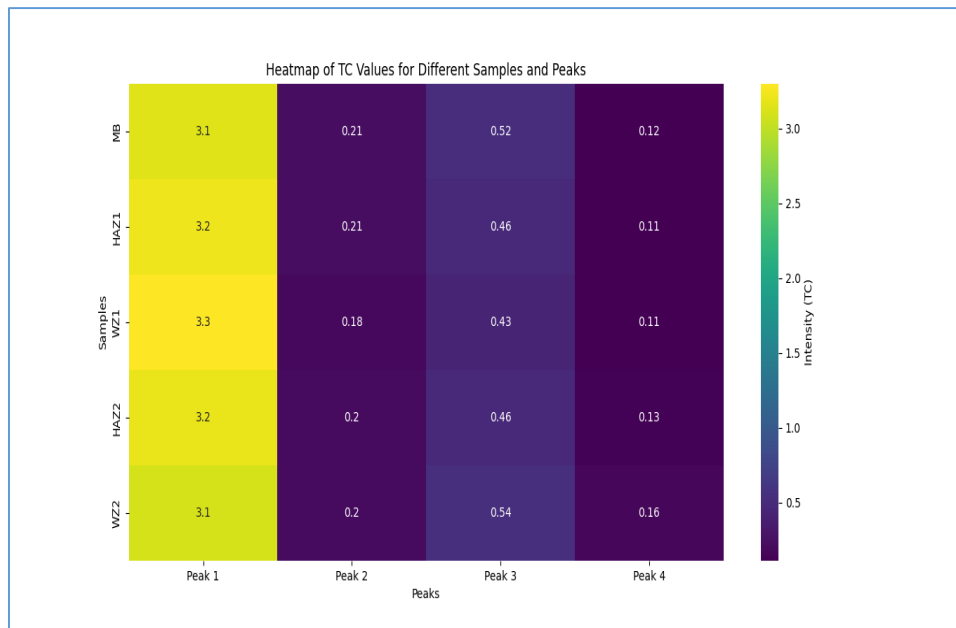**Figure IV.4:** Color map of crystal texture coefficients (TC) distribution across different peaks in X-ray Analysis at two welding speeds**.**
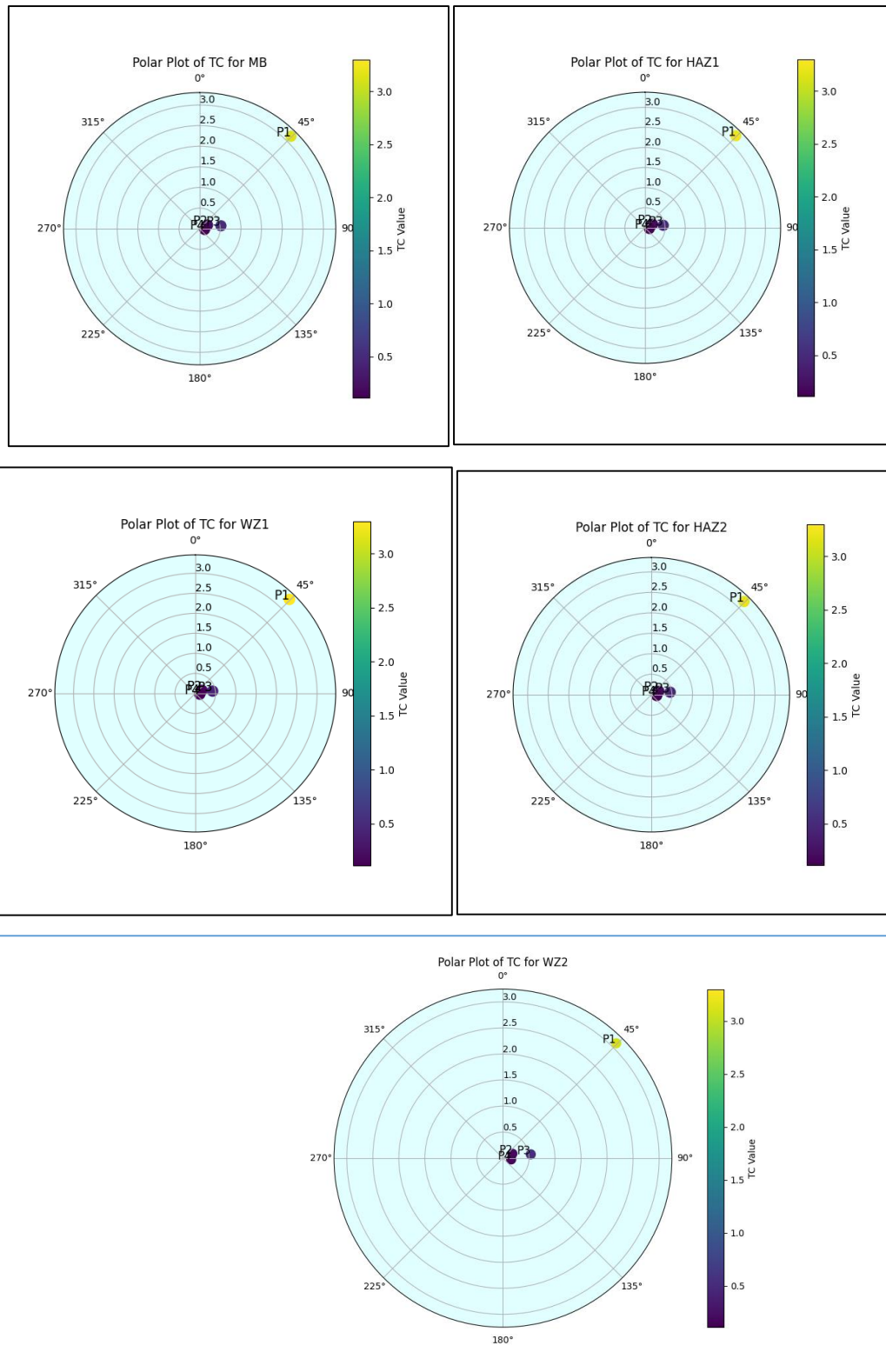
Figure IV.5: polar plot of crystal texture coefficient (TC) distribution at two welding speeds**.**

❖ **Analysis of results**

In this analysis, the Texture Coefficient **(TC)** results for two different welding speeds were assessed, with a focus on how each speed affects the distribution of crystal orientation across various welding zones **(HAZ, WZ, and MB)**. To ensure a more detailed and precise evaluation, the findings were organized into three main sections:

⬦ **Analysis of Texture Coefficient (TC) Results for the Two Welding Speeds**

First speed (HAZ$_1$, WZ$_1$ and MB)

Based on the data from the table, color maps, and polar plots of texture coefficient distributions, the welding zones at the initial speed **(HAZ$_1$, WZ$_1$, MB)** exhibit relatively high texture coefficients at **peak 1**. Notably, the texture coefficient at **peak 1** for **WZ$_1$** is **3.3**, the highest observed among all peaks. This suggests a significant alignment of crystal orientations in these directions, indicating that the crystal structure in these regions is likely more stable and uniform**.**

Second speed (HAZ$_2$, WZ$_2$ and MB)

At the second speed, the texture coefficient values at **Peak 1** remain high, though they are slightly lower than those observed at the first speed. For instance, the texture coefficient in **WZ2** is **3.1.** While there is still a noticeable preference for crystal orientation at this speed, the reduction in the texture coefficient compared to the first speed suggests that the faster cooling rate may affect crystal alignment or potentially increase defects in these regions**.**

⬦ **Analysis across different vertices (Peak1, Peak 2, Peak 3 and Peak 4)**

The low texture coefficient **(TC)** values at **Peak 2, Peak 3, and Peak 4** across all samples suggest that the crystal orientations in these directions are less favorable. For instance, the **TC** at **Peak 2** ranges from **0.18 to 0.21** at the first speed and is approximately **0.2** at the second speed. This indicates that the crystal structure in these orientations is less uniform, potentially increasing the material's susceptibility to defects or deformations**.**

⬦ **Correlation with angles 2 θ and HKL**

The consistent **hkl** values and **2θ** angles across different samples indicate that the fundamental crystal structure of the material remains stable despite the welding process. However, slight variations in the texture coefficient **(TC)** values among the samples suggest differences in the internal crystal orientation in specific directions, likely resulting from the effects of rapid or slow cooling**.**

❖ **Interpretation of results**

At the first welding speed, crystal cohesion is notably strengthened in the primary directions, pointing to a more stable crystal structure in the affected areas. In contrast, at the second speed, despite the preservation of the fundamental crystal orientation, rapid cooling appears to introduce additional defects or reduce crystal regularity, leading to a decrease in the Texture Coefficient **(TC)**.

The lower **TC** values observed at **Peaks 2, 3, and 4** reflect increased irregularities in crystal alignment, which may negatively impact the material's properties. Although the consistent **hkl** values and **2θ** angles across samples confirm that the basic crystal structure remains intact, the slight variations in **TC** values underscore the impact of cooling rates on internal crystal orientation, which ultimately affects the material's overall characteristics **(A.Wauthier-Monnin et al., 2015)(S. Rahimi et al., 2019)(R. Badji et al., 2013)(Thuvander et al., 2007)(.K. Patel et al., 2013)(M. Safaeirad et al., 2008).**

❖ **Conclusion**

The analysis shows that a slower welding speed **(S$_1$ = 20 mm/min)** enhances the texture coefficient at Vertex 1, indicating a more stable crystal structure and improved welding quality. Conversely, a higher speed **(S$_2$ = 35 mm/min)** causes a slight reduction in texture coefficients, likely due to rapid cooling, which increases crystal defects and may adversely affect welding quality. Thus, welding speed has a notable effect on crystal orientation distribution in **X70** steel, with potential implications for the material's properties**.**

Conclusion

This study provides a comprehensive analysis of the effects of welding speed on the microstructural and mechanical properties of X42 steel welded using the Shielded Metal Arc Welding (SMAW) process. By employing various analytical techniques, including X-ray diffraction (XRD), hardness testing (Vickers and Brinell), and Scanning Electron Microscopy (SEM), the study has demonstrated that welding speed significantly influences the crystallinity, dislocation density, grain structure, and overall mechanical performance of the welded material.

The findings highlight that lower welding speeds (S1 = 20 mm/min) promote a more stable crystal structure, characterized by larger and more uniform crystals. This stability results in enhanced weld quality, reduced dislocation density, and improved mechanical properties, such as increased strength and resistance to fracture. Additionally, slower speeds contribute to broader grain growth and a clearer formation of mixed ferrite and carbide phases in the heat-affected zones (HAZ). However, the extended cooling time associated with lower speeds can lead to a slight reduction in hardness due to prolonged exposure to heat.

Conversely, higher welding speeds (S2 = 35 mm/min) lead to rapid cooling, which disrupts crystal stability, increases dislocation density, and introduces defects due to insufficient time for grain refinement. This results in a more brittle structure with reduced ductility and greater variability in hardness across different weld regions. The SEM analysis further reveals that higher speeds create more defined interstitial structures, leading to reduced variability in ferrite content and an increased likelihood of internal stresses. Additionally, faster cooling limits carbon migration and oxidation in the heat-affected zones, preserving the chemical composition closer to that of the base metal, but at the cost of increased hardness fluctuations and a more pronounced anisotropic grain orientation.

The hardness analysis confirms that welding speed directly impacts the uniformity of heat distribution, with slower speeds ensuring a more even hardness profile, while higher speeds induce localized hard and brittle phases due to thermal inconsistencies. The variations in texture coefficient (TC) values further indicate that welding speed influences internal crystal orientation, with slower speeds enhancing texture stability and higher speeds causing distortions.

Moreover, the study demonstrates that welding speed affects fine material distribution in welded steel. Slower speeds promote denser particle formations, leading to a compact and stronger microstructure, while higher speeds result in lower particle density and larger grains, particularly in the heat-affected zones. This influences the material's rigidity and elasticity, emphasizing the importance of welding speed in optimizing mechanical performance.

Overall, the results suggest that an optimal welding speed should balance the advantages of both slow and fast welding. While lower speeds improve structural integrity and mechanical stability, they can slightly reduce hardness. On the other hand, higher speeds enhance productivity but introduce structural defects and variability in mechanical properties. Therefore, a moderate welding speed—between 20 mm/min and 35 mm/min—may offer the best trade-off between weld quality and production efficiency.

To mitigate the negative effects of rapid cooling, advanced techniques such as controlled cooling, laser welding, or optimized arc welding methods should be considered. Further research should focus on refining welding parameters and employing advanced thermal analysis techniques to better understand and control heat distribution within the weld zones.

 In conclusion, welding speed is a critical parameter that directly influences the microstructural and mechanical behavior of welded X70 steel. By carefully selecting and controlling the welding speed, it is possible to optimize weld quality, enhance material performance, and ensure the long-term reliability of welded structures in industrial applications.

References

.K. Patel, D. Bhole, L. C. (2013). Formation of zinc interlayer texture during dissimilar ultrasonic spot welding of magnesium and high strength low alloy steel. *Materials and Design*, *45*, 236–240. https://doi.org/10.1016/j.matdes.2012.09.018

A. Mebrek, S. Alleg, S. Souilh, R. Hamrouni, S. A. (2013). *Etude des propriétés mécaniques et structurales des pipelines , Grade X42*. 2–5.

A. Ravisankar, K. Satish , R. Gaurav, S. V. (2014). Influence of welding speed and power on residual stress during gas tungsten arc welding (GTAW) of thin sections with constant heat input: A study using numerical simulation and experimental validation. *Journal of Manufacturing Processes*, *16*(2), 200–211. https://doi.org/10.1016/j.jmapro.2013.11.002

A.Mouloud. (2003). *Étude Du Comportement Thermique Et Mecanique Des Materiaux Aeronautiques Par Des Methodes Numeriques : Application Au Soudage De Structures Metalliques*.

A.safa, CH.Nedjema, G. kenz. (2024). *Study of the effect of SMAW welding speed on the microstructure and crystal stability of X70 steel using X-ray diffraction Estudo do efeito da velocidade de soldagem SMAW na microestrutura e estabilidade cristalina do aço X70 usando difração de raios X Es*. 1–21. https://doi.org/10.54021/seesv5n2-391

A.Wauthier-Monnin, T. Chauveau, O. Castelna, H. Réglé, B. B. (2015). The evolution with strain of the stored energy in different texture components of cold-rolled if steel revealed by high resolution X-ray diffraction. *Materials Characterization*, *104*, 31–41. https://doi.org/10.1016/j.matchar.2015.04.005

Adnen, K. (2013). *Faculté des Sciences Appliquées ETUDE DU SOUFFLAGE MAGNETIQUE DE L ' ARC ELECTRIQUE DE SOUDAGE Thèse de Doctorat Présentée par Adnen KECHAOU*.

B. Maalache, M.Bouabdallah, Y.Yahmi, B.Cheniti, B. M. (2018). *X-Ray Diffraction Evaluation of Dislocation Density and Crystallite Size in the HAZ*. 1–7.

B.Hadjer. (2022). *Thème Modélisation des procédés de soudage : Application aux assemblages des pipelines*.

B.Hichem. (2013). *Optimisation de la vitesse de soudage a l'arc électrique des aciers*.

B.Ismail. (2017). *Détermination des différents critères de qualité des joints soudés sur les pipelines en service. Université Abou Bekr Belkaïd – Tlemcen Faculté*.

B.Lotfi, H. S. (2018). *Elaboration et caractérisation des joints soudés des aciers Soutenu*. UNIVERSITE MOHAMED BOUDIAF - M'SILA.

B.Luis, D.Sumeet, S. S. (2011). Engineering Properties of Polymeric-Based Antimicrobial Films for Food Packaging. *Food Engineering Reviews*, *3*(2), 79–93. https://doi.org/10.1007/s12393-011-9034-8

B.Mostefa. (2012). *Étude les défauts de soudage des pipelines Présenté*.

B.Yassine. (2016). *Option : Génie chimique Etude comparative entre deux procédés de soudage des pipelines Présentée par : BARKAT YASSINE*. Université Mohamed Khider Biskra.

Bachir, M. (2015). *Titre :Etude de l'influence des paramètres de soudage sur la microstructure et le comportement mécanique des assemblages acier-aluminium obtenu par soudage à l'arc MIG-CMT*. Université Montpellier; Université Abou Bekr Belkaid.

C. Atilla,E. Nasuf, N. B. (2004). The assessment of rock cutability, and physical and mechanical rock properties from a texture coefficient. *Journal of The South African Institute of Mining and Metallurgy*, *104*(7), 397–402.

CH.Julien. (2011). *Une approche pour l'optimisation des opérations de soudage à l'arc To cite this version : `SE Une approche pour l'optimisation des op´erations de soudage a `l'arc*.

CH.Nedjema. (2015). *Effet du soudage par TIG sur l'aluminium industriel 1050A*. Université Mohamed Khider - Biskra.

CH.Soumya, S. K. (2017). Role of crystallographic texture, delamination and constraint on anisotropy in fracture toughness of API X70 line pipe steels. *Materials Science and Engineering: A*, *708*, 254–266. https://doi.org/10.1016/j.msea.2017.09.104

D.Arnaud. (2019). *Simulations massives de Dynamique des Dislocations : fiabilité et performances sur architectures parallèles et To cite this version : HAL Id : tel-02012109 L'UNIVERSITÉ DE BORDEAUX*.

D.Boualem, & Le. (2020). *Résine de Schinus molle comme inhibiteur vert pour l'acier API 5L X70 en milieu HCl 5 %*. 2019–2020.

Das Bakshi, S., Dhande, T., Javed, N., Sasidhar, K. N., Sharma, V., Mukherjee, M., Ghosh, B., & Mahashabde, V. V. (2019). Effect of hot deformation and crystallographic texture on toughness anisotropy and fracture behavior of Nb+V microalloyed API X70 steel. *International Journal of Pressure Vessels and Piping*, *171*(February), 162–172. https://doi.org/10.1016/j.ijpvp.2019.02.016

E. Curiel-Reyna, A. Herrera, V. Castaño, E. R. (2006). Influences of the precooling treatment in the heat affected zone of the welding in a used hadfield-type steel. *Materials and Manufacturing Processes*, *21*(5), 573–578. https://doi.org/10.1080/10426910600599380

G. Chukhchin,V. Malkov,V. Tyshkunova,V. Mayer, V. N. (2016). Diffractometric method for determining the degree of crystallinity of materials. *Crystallography Reports*, *61*(3), 371–375. https://doi.org/10.1134/S1063774516030081

G. Leyi, J. Zhou., S. H. (2011). Mechanics analysis and simulation of material Brinell hardness measurement. *Measurement: Journal of the International Measurement Confederation*, *44*(10), 2129–2137. https://doi.org/10.1016/j.measurement.2011.07.024

G. Sandomirskii. (2017). Estimation of the Ultimate Tensile Strength of Steel from Its HB and HV Hardness Numbers and Coercive Force. *Russian Metallurgy (Metally)*, *2017*(11), 989–993. https://doi.org/10.1134/S003602951711012X

G. Tong, C. Gu, W. Yin, L. Wang, W. B. (2016). Impacts of torch moving on phase change and fluid flow in weld pool of SMAW. *International Journal of Heat and Mass Transfer*, *100*, 949–957. https://doi.org/10.1016/j.ijheatmasstransfer.2016.04.032

G.Olfa. (2015). *Amélioration des propriétés physico-chimiques et anticorrosives du revêtement de polypyrrole électrodéposé sur l'acier inoxydable 304*.

G.Pasqualino, E.Vincenzo, G.Eugenio, M. A. (2018). Full-field analysis of AL/FE explosive welded joints for shipbuilding applications. *Marine Structures*, *57*(June 2017), 207–218. https://doi.org/10.1016/j.marstruc.2017.10.004

H.Féthi. (2013). Thème Etude du comportement en fatigue des aciers pour pipelines à différents grades. *Thése Doctorat*, 2012–2013.

Halim, Z. A. (2020). *Etude du comportement hydrodynamique du bain liquide lors du soudage à 'larc éléctrique*. UNIVERSITÉ SAAD DEHLEB DE BLIDA.

Hanifa, M. (2012). *Caractérisation structurale et mécanique du joint soudé de la liaison bimétallique Acier Ordinaire E36/ Acier anti-usure NAXTRA70 utilisé par l'Unité Grue de Bejaïa dans l'assemblage de la pelle chargeuse et godet d'excavation Présenté*. Université Mouloud Mammeri de Tizi-Ouzou.

Herrera, E. Curiel-Reyna, M. Castaño, E. R. (2005). Influence of cooling rate on the structure of heat affected zone after welding a high manganese steel. *Materials and Manufacturing Processes*, *20*(5), 813–822. https://doi.org/10.1081/AMP-200055142

Houda, Y. (2013). *Influence of scale parameters of pearlite on the kinetics of anisothermal pearlite-to austenite transformation in a eutectoid steel. Thèse de doctorat, ParisTech* (Issue Umr 8006). l'École Nationale Supérieure d'Ingénieurs de Tunis.

J. Rohit, K. J. (2014). Influence of Welding Current and Joint Design on the Tensile Properties of SMAW Welded Mild Steel Joints. *Journal of Engineering Research and Applications Www.Ijera.Com*, *4*(6), 106–111. www.ijera.com

Jha, J. R. (2014). Investigating the Effect of Welding Current on the Tensile Properties of SMAW Welded Mild Steel Joints. *International Journal of Engineering Research & Technology*, *3*(4), 1304–1307. www.ijert.org

K. Bijaya, S.Soumya, K. Swapan, B. B. (2020). Effect of welding parameters on mechanical and microstructural properties of GMAW and SMAW mild steel joints. *Ironmaking and Steelmaking*, *47*(8), 844–851. https://doi.org/10.1080/03019233.2019.1623592

K.Chaima. (2020). *Effet de traitement thermique sur la qualité d ' un acier ordinaire*. Université Mohamed Khider de Biskra.

K.Nitin, K. Rangasayee, L. Leijun, A. Neil, R. Muhammad, C. Laurie, D. JONA, W .Popla, U. R. (2021). A Mechanism for Carbon Depletion at Bondline of High-Frequency Electric-Resistance-Welded X70 Pipeline Steel. *Metallurgical and Materials Transactions A: Physical Metallurgy and Materials Science*, *52*(9), 3788–3798. https://doi.org/10.1007/s11661-021-06339-w

K.Noureddine. (2007). *Etude par diffraction des rayons X in situ des mécanismes d'oxydation de l'acier AISI 304 entre 800°C et 1000°C. Influence des dépôts sol-gel de lanthane et de cérium. Apport de la spectroscopie infrarouge a l'identification des oxydes mixtes.*

Karuhanga, B. N. (2010). Characterization of the fracture behaviour of X42 microalloyed pipeline steel. *The Eletronic Library*, *34*(1), 1–5.

KH.Farida. (2017). *Thème Influence du flux de soudage sur la qualité de la soudure des Pipelines*. BADJI MOKHTAR-ANNABA UNIVERSITY.

L.Shibo. (2017). *Numerical and experimental study on residual stresses in laser beam welding of dual phase DP600 steel plates Numerical and experimental study on residual stresses in laser beam welding of dual phase DP600 steel plates*.

M. Ali, M. Mouatez Billah, B. E. (2020). *Identification expérimentale des caractéristiques mécaniques de l acier X70 D ALFAPIPE - PDF Free Download.pdf*.

M. Birkholz. (2007). Modelling of diffraction from fibre texture gradients in thin polycrystalline films. *Journal of Applied Crystallography*, *40*(4), 735–742. https://doi.org/10.1107/S0021889807027240

M. Mohammad, C.Cleiton, F. H. (2017). Effect of rolling in the recrystallization temperature region associated with a post-heat treatment on the microstructure, crystal orientation, and mechanical properties of API 5L X70 pipeline steel. *Materials Research*, *20*(1), 151–160. https://doi.org/10.1590/1980-5373-MR-2016-0651

M. Mohammad, F. Luis, F. H. (2015). Study of texture and microstructure evaluation of steel API 5L X70 under various thermomechanical cycles. *Materials Science and*

Engineering: A, *639*, 550–558. https://doi.org/10.1016/j.msea.2015.05.020

M. Mostafavi, M. Collins, B. Cai, R. Bradley, C. Atwood, C. Reinhard, X. Jiang, M. Galano, D. Lee, J. M. (2015). Yield behavior beneath hardness indentations in ductile metals, measured by three-dimensional computed X-ray tomography and digital volume correlation. *Acta Materialia*, *82*, 468–482. https://doi.org/10.1016/j.actamat.2014.08.046

M. Rashidi, M. Hayati, A. R. (2011). Prediction of the relative texture coefficient of nanocrystalline nickel coatings using artificial neural networks. *Solid State Sciences*, *13*(8), 1589–1593. https://doi.org/10.1016/j.solidstatesciences.2011.06.005

M. Safaeirad, R. Toroghinejad, F. A. (2008). Effect of microstructure and texture on formability and mechanical properties of hot-dip galvanized steel sheets. *Journal of Materials Processing Technology*, *196*(1–3), 205–212. https://doi.org/10.1016/j.jmatprotec.2007.05.035

M.Biezma, A.Andrés, D.Agud, E. B. (2020). Most fatal oil & gas pipeline accidents through history: A lessons learned approach. *Engineering Failure Analysis*, *110*(August 2019), 1–14. https://doi.org/10.1016/j.engfailanal.2020.104446

M.Hayat. (2017). Amélioration de la résistance à la corrosion électrochimique des aciers par utilisation des inhibiteurs. In *These*. UNIVERSITE MOHAMED KHIDER-BISKRA Faculté.

M.Hichem. (2017). *DÉVELOPPEMENT DE NUANCES D'ACIER AU MANGANESE ALLIE DESTINE A L'USURE*.

M.Majeed, M.Mohammed, S. S. (2013). *X-Ray Mass Attenuation Coefficients of Some 3D Elements Compounds at Am-241(40mCi) International Review of Physics (IREPHY)*. *241*(June 2016). https://www.researchgate.net/publication/304247578

M.Quentin. (2020). *Modélisation de la macrostructure de soudures TIG épaisses multipasses en acier inoxydable austénitique. Application au contrôle ultrasonore de soudures du circuit primaire des RNR-Na*. Aix-Marseille Université.

M.Younes, H. A. (2014). *Contrôle qualité des soudures X52M réalisées par les procèdés SAW et SMAW*. Université Mouloud Mammeri de Tizi-Ouzou.

N. Jerzy, R. P. (2005). The influence of welding heat input on submerged arc welded duplex steel joints imperfections. *Journal of Materials Processing Technology*, *164–165*, 1082–1088. https://doi.org/10.1016/j.jmatprotec.2005.02.079

N. JiaF. Shen, W. Liang, W. Feng, B. Wang, K. M. (2017). Nanoscale spheroidized cementite induced ultrahigh strength-ductility combination in innovatively processed ultrafine-grained low alloy medium-carbon steel. *Scientific Reports*, *7*(1), 1–9.

57

https://doi.org/10.1038/s41598-017-02920-9

Özarpa, C., Akkuş, A., & Kınacı, B. F. (2023). Investigation on the mechanical properties of X42N, grade A and grade B steel pipes joined by shielded metal arc and TIG welding. *Journal of the Faculty of Engineering and Architecture of Gazi University*, *38*(2), 963–974. https://doi.org/10.17341/gazimmfd.1068748

P. Tewari, G. Ankur, P. J. (2010). Effect of Welding Parameters on the Weldability of Material. */ International Journal of Engineering Science and Technology*, *2*(4), 512–516.

R. BadjiT. Chauveau, B. B. (2013). Texture, misorientation and mechanical anisotropy in a deformed dual phase stainless steel weld joint. *Materials Science and Engineering: A*, *575*, 94–103. https://doi.org/10.1016/j.msea.2013.03.018

R. Bodlos. (2018). *Detailed microstructure characterization of a grade X70 steel modified with TiO2 using friction stir processing* (Issue July). Graz University of Technology Supervisor:

R. Eslam, H. Stefanie, W. Sabine, F. A. (2012). Effect of welding parameters on the heat-affected zone of AISI409 ferritic stainless steel. *International Journal of Minerals, Metallurgy and Materials*, *19*(10), 923–929. https://doi.org/10.1007/s12613-012-0648-5

S. Chakrabarti, D. Ganguli, S. C. (2004). Substrate dependence of preferred orientation in sol-gel-derived zinc oxide films. *Materials Letters*, *58*(30), 3952–3957. https://doi.org/10.1016/j.matlet.2004.09.002

S. Farrukh, M. Quazi, J.Bhatti,M. Nasir, I. . A. (2019). Effect of Shielded Metal Arc Welding (SMAW) parameters on mechanical properties of low-carbon, mild and stainless-steel welded joints: A review. *Journal of Advances in Technology and Engineering Research*, *5*(5), 191–198. https://doi.org/10.20474/jater-5.5.1

S. Kumar, A. S. (2011). Effect of heat input on the microstructure and mechanical properties of gas tungsten arc welded AISI 304 stainless steel joints. *Materials and Design*, *32*(6), 3617–3623. https://doi.org/10.1016/j.matdes.2011.02.017

S. Rafael, T. Michael, S. Nina, P. Marianne, C. Christoph, M. C. (2019). Effects of reference materials on texture coefficients determined for a CVD α-Al2O3 coating. *Surface and Coatings Technology*, *359*, 314–322. https://doi.org/10.1016/j.surfcoat.2018.12.095

S.Aqida, D.Brabazon, S. N. (2013). An investigation of phase transformation and crystallinity in laser surface modified H13 steel. *Applied Physics A: Materials Science and Processing*, *110*(3), 673–678. https://doi.org/10.1007/s00339-012-7149-2

S.Mounir. (2017). *Synthèse , élaboration et caractérisation des nanocomposites à base de magnésium pour le stockage solide d ' hydrogène Mounir Sahli To cite this version :*

HAL Id : tel-01505959 Présentée pour obtenir le diplôme de doctorat en sciences en Physique Spéciali.

S.Rahimi , T.N. Konkova, I. Violatos, N. B. (2019). Evolution of Microstructure and Crystallographic Texture During Dissimilar Friction Stir Welding of Duplex Stainless Steel to Low Carbon-Manganese Structural Steel. *Metallurgical and Materials Transactions A: Physical Metallurgy and Materials Science*, *50*(2), 664–687. https://doi.org/10.1007/s11661-018-5023-3

Sablik, M. J. (2001). Modeling the effect of grain size and dislocation density on hysteretic magnetic properties in steels. *Journal of Applied Physics*, *89*(10), 5610–5613. https://doi.org/10.1063/1.1359167

SH.Satish, M. S. (2017). A review on welding of high strength oil and gas pipeline steels. *Journal of Natural Gas Science and Engineering*, *38*, 203–217. https://doi.org/10.1016/j.jngse.2016.12.039

T. Atsushi, K. Yu Ichi , T. Hidenori, Y. T., & Oi, Kenji, Y. K. (2015). Crystallographic analysis for acicular ferrite formation in low carbon steel weld metals. *Welding International*, *29*(4), 254–261. https://doi.org/10.1080/09507116.2014.921042

T. Shintani, Y. M. (2011). Evaluation of the dislocation density and dislocation character in cold rolled Type 304 steel determined by profile analysis of X-ray diffraction. *Acta Materialia*, *59*(11), 4314–4322. https://doi.org/10.1016/j.actamat.2011.03.055

T. UngaÂr, J. Gubicza, G. RibaÂrik, A. B. (2001). Crystallite size distribution and dislocation structure determined by diffraction profile analysis : principles and practical application to cubic and hexagonal crystals research papers Crystallite size distribution and dislocation structure determined by. *Journal of Applied Crystallography*, 298–310.

Thuvander, M. GustafssonM.L. Bergqvist, E. Keehan, L. K. (2007). Effect of welding procedure on texture and strength of nickel based weld metal. *Science and Technology of Welding and Joining*, *12*(6), 549–555. https://doi.org/10.1179/174329307X213800

V. Kolubaev, V. Sizova, V. Fortuna, N. Ivanov, A. K. (2020). Weld structure of low-carbon structural steel formed by ultrasonic-assisted laser welding. *Journal of Constructional Steel Research*, *172*, 106190. https://doi.org/10.1016/j.jcsr.2020.106190

V. Uvarov, I. P. (2007). Metrological characterization of X-ray diffraction methods for determination of crystallite size in nano-scale materials. *Materials Characterization*, *58*(10), 883–891. https://doi.org/10.1016/j.matchar.2006.09.002

Vahid, H. (2016). Influence of multi-pass welding on the microstructure evolution and corrosion resistance of a super duplex stainless steel. In *International Journal of*

Electrochemical Science (Vol. 11, Issue 11). https://doi.org/10.20964/2016.11.28

W. Bo, X. Songbai, M. Chaoli, W. Jianxin, L. Z. (2017). Effects of porosity, heat input and post-weld heat treatment on the microstructure and mechanical properties of TIG welded joints of aa6082-t6. *Metals*, *7*(11). https://doi.org/10.3390/met7110463

W. Li, V.Martina, J. Geurt, S. J. S. (2020). The combined influence of grain size distribution and dislocation density on hardness of interstitial free steel. *Journal of Materials Science and Technology*, *45*, 35–43. https://doi.org/10.1016/j.jmst.2019.11.025

W. Sowards, C. Lippold, W. Dickinson, J. R. (2008). Characterization of welding fume from SMAW electrodes - Part I. *Welding Journal (Miami, Fla)*, *87*(4).

W. Sutapa, A. Wahid, P. Taba, L. N. (2018). Dislocation, crystallite size distribution and lattice strain of magnesium oxide nanoparticles. *Journal of Physics: Conference Series*, *979*(1). https://doi.org/10.1088/1742-6596/979/1/012021

W. Yaqin, T. Wu, Z. L. (2015). Crystalline Size Effects on Texture Coefficient, Electrical and Optical Properties of Sputter-deposited Ga-doped ZnO Thin Films. *Journal of Materials Science and Technology*, *31*(2), 175–181. https://doi.org/10.1016/j.jmst.2014.11.009

X.Yang, B. Kan, X. Li, J. SU, J. Q. (2018). Hydrostatic pressure effects on corrosion behavior of X70 pipeline steel in a simulated deep-sea environment. *Journal of Electroanalytical Chemistry*, *822*(November 2017), 123–133. https://doi.org/10.1016/j.jelechem.2018.05.010

Xiongjie, L. (2013). *Développement de la caractérisation du comportement local à haute température des alliages métalliques par micrro indentation*. Université de Technologie de Compiègne Laboratoire.

Yusof, E. M. M., Yusof, M. I., Ali, R., Harjimi, I. H., & Bahrin, Q. K. (2020). Welding station monitoring system using internet of thing (IoT). *Indonesian Journal of Electrical Engineering and Computer Science*, *18*(3), 1319–1330. https://doi.org/10.11591/ijeecs.v18.i3.pp1319-1330

Z. idani, F. Khamouli, K. Digheche, A. Saoudi, H. Moussi, L. A. (2019). Chemical characterization of the crystalline phases in agglomerated fluxes and slags for shielded metal arc welding (SMAW). *Solid State Phenomena*, *297*, 151–164. https://doi.org/10.4028/www.scientific.net/SSP.297.151